

AD

AD-E403 218

Technical Report ARWSE-TR-09004

ELECTROMAGNETIC (EM) WAVE ATTACHMENT TO LASER PLASMA FILAMENTS

D. Clint Friedman

May 2009



U.S. ARMY ARMAMENT RESEARCH, DEVELOPMENT AND
ENGINEERING CENTER

Weapons and Software Engineering Center

Picatinny Arsenal, New Jersey

Approved for public release; distribution is unlimited.

20090610633

The views, opinions, and/or findings contained in this report are those of the author(s) and should not be construed as an official Department of the Army position, policy, or decision, unless so designated by other documentation.

The citation in this report of the names of commercial firms or commercially available products or services does not constitute official endorsement by or approval of the U.S. Government.

Destroy this report when no longer needed by any method that will prevent disclosure of its contents or reconstruction of the document. Do not return to the originator.

REPORT DOCUMENTATION PAGE

Form Approved
OMB No. 0704-01-0188

The public reporting burden for this collection of information is estimated to average 1 hour per response, including the time for reviewing instructions, searching existing data sources, gathering and maintaining the data needed, and completing and reviewing the collection of information. Send comments regarding this burden estimate or any other aspect of this collection of information, including suggestions for reducing the burden to Department of Defense, Washington Headquarters Services Directorate for Information Operations and Reports (0704-0188), 1215 Jefferson Davis Highway, Suite 1204, Arlington, VA 22202-4302. Respondents should be aware that notwithstanding any other provision of law, no person shall be subject to any penalty for failing to comply with a collection of information if it does not display a currently valid OMB control number.

PLEASE DO NOT RETURN YOUR FORM TO THE ABOVE ADDRESS.

1. REPORT DATE (DD-MM-YYYY) May 2009	2. REPORT TYPE Final	3. DATES COVERED (From - To) 2008		
4. TITLE AND SUBTITLE ELECTROMAGNETIC (EM) WAVE ATTACHMENT TO LASER PLASMA FILAMENTS		5a. CONTRACT NUMBER		
		5b. GRANT NUMBER		
		5c. PROGRAM ELEMENT NUMBER		
6. AUTHORS D. Clint Friedman		5d. PROJECT NUMBER		
		5e. TASK NUMBER		
		5f. WORK UNIT NUMBER		
7. PERFORMING ORGANIZATION NAME(S) AND ADDRESS(ES) U.S. Army ARDEC, WSEC Weapons Systems & Technology Directorate (RDAR-WSW-A) Picatinny Arsenal, NJ 07806-5000		8. PERFORMING ORGANIZATION REPORT NUMBER		
9. SPONSORING/MONITORING AGENCY NAME(S) AND ADDRESS(ES) U.S. Army ARDEC, ESIC Knowledge & Process Management Office (RDAR-EIK) Picatinny Arsenal, NJ 07806-5000		10. SPONSOR/MONITOR'S ACRONYM(S)		
		11. SPONSOR/MONITOR'S REPORT NUMBER(S) Technical Report ARWSE-TR-09004		
12. DISTRIBUTION/AVAILABILITY STATEMENT Approved for public release; distribution is unlimited.				
13. SUPPLEMENTARY NOTES				
14. ABSTRACT This report explores the theoretical and experimental analysis of using plasma filaments generated by a femtosecond class laser system as a means for transmission of radio frequency (RF) electromagnetic (EM) waves. Theoretically, the plasma filaments are modeled as complex cylindrical wires in space for single and dual wire configurations. Attenuation as a function of distance is calculated for single wire transverse electric mode propagation and dual wire transverse electromagnetic (TEM) mode propagation. Minimum attenuation is shown to be dependent on filament diameter, electron density, and filament separation (for the dual wire case). Initial experimental validation of theoretical models is performed with copper wire filament surrogates. Radio frequency/plasma filament interaction is then demonstrated in a rectangular waveguide fixture. Filament electron density enhancement is demonstrated in cylindrical resonant RF cavities (2.6 GHz and 0.9 GHz) where an increase in pulse width of attached EM waves beyond lifetimes of typical ultrafast laser generated plasma filaments is observed. Transmission of RF energy out of resonant cavities along a filament is demonstrated further validating transmission theory.				
15. SUBJECT TERMS Filamentation, Radio frequency (RF), Electromagnetic (EM) waves, Femtosecond, Ultra-fast laser, and Microwave cavity				
16. SECURITY CLASSIFICATION OF: a. REPORT U b. ABSTRACT U c. THIS PAGE U		17. LIMITATION OF ABSTRACT SAR	18. NUMBER OF PAGES 51	19a. NAME OF RESPONSIBLE PERSON D. Clint Friedman 19b. TELEPHONE NUMBER (Include area code) (973) 724-5174

CONTENTS

	Page
Introduction	1
Optical Filamentation	1
Self Channeling - Filamentation	1
Phenomenology	2
Kerr Self-Focusing	2
Propagation through the atmosphere	3
Ultrafast Lasers	5
Broad Band is Ultrashort	5
Chirped Pulse Amplification	5
Peak Powers, Intensities	8
Filament Interaction with Electromagnetic Waves	9
Filament Conductivity	9
Radio Frequency Interaction	9
Ultrafast Laser Filament/Radio Frequency Interaction	10
Experimental Setup	11
Laser	11
Radio Frequency Sources	11
Detection and Measurement Equipment	12
Experiments	13
Single Wire Propagation (Copper)	13
Two Wire Propagation	15
Rectangular Waveguide Interaction	16
Resonant Cavity Interaction	18
Planned Follow-up: Free Space Filament/Open-ended Rectangular Waveguide Attachment	26
Theory and Modeling	26
Basic Theory	26
Single Wire Filament	27
Two Plasma Wires	33
Conclusions and Summary	40
References	43
Distribution List	45

FIGURES

	Page
1 Filament formation	4
2 Pulse compression grating	6
3 Lab system compressor beam path	6
4 Regenerative amplifier	7
5 Multi-pass amplifier	8
6 TW amplifier	8
7 RF linear amplifier gain plot	12
8 Single wire (copper) propagation layout	13
9 Single copper wire propagation	14
10 Normalized single copper wire propagation	15
11 Dual copper wire RF propagation	16
12 Rectangular waveguide fixture	17
13 Rectangular waveguide interaction	18
14 Cylindrical resonant cavity (cavity A)	19
15 Q, cavity A	20
16 Cavity A, short focus attachment	21
17 Cavity A, long focus attachment	23
18 Q, cavity B	24
19 Cavity B, field resonance	24
20 Cavity B, short focus attachment	25
21 Cavity B, long focus attachment	25
22 Wire, cylindrical coordinates	27
23 Air/plasma interface	32
24 Dispersion versus $Reh\lambda_0$, $Imh\lambda_0$	32
25 Coupled versus free-space propagation	33

FIGURES
(continued)

	Page
26 Dual wire geometry	34
27 Dual wire attenuation as a function of electron density	38
28 Dual wire attenuation as a function of frequency	38
29 Dual wire attenuation as a function of wire diameter	39
30 Dual wire attenuation as a function of wire separation	39
31 Attenuation as a function of electron density for feasible ideal cases	40

INTRODUCTION

Not long after the development of the laser in the early 1960s, scientists demonstrated that a laser with modest power could be focused sharply in order to create plasma in the air. However, not until the development of “ultrashort” pulsed lasers and their surge in popularity in the late 1980s, was a phenomena known as optical filamentation discovered. Optical filamentation is distinguished from the plasma regions typical of conventional high power lasers, in that it is not created solely by, nor restricted to, the optical focus. Optical filaments do not immediately diverge; rather represent an ionized pathway created in the wake of the laser beam. This ionized plasma pathway, or filament as it is often referred to, has opened up a new realm of possibilities for scientific exploration. This opens the door to vast commercial, medical, and military applications.

In this report, the physics of this ionized pathway and attempt to use it as a means of delivering radio frequency (RF) radiation was examined. Various potential methods of RF attachment to the plasma channel are examined and their effectiveness through both FDTD models and laboratory experiments in order to optimize this interaction was studied. The results demonstrated the feasibility and requirements for RF attachment both in terms of laser pulse characteristics and RF parameters. A number of scenarios including varied filament characteristics and geometries as well as RF frequencies and power levels were explored. The coupling of various RF propagation modes in both waveguide and in free-space in an attempt to determine the optimum configuration for coupling of an RF pulse to a filament or number of filaments, for maximum received power over distance was looked at.

With an improved understanding of RF/filament interaction, it may be possible to demonstrate an increase in RF transmission range for free-space propagation through the atmosphere given a fixed RF input power. Overcoming the conventional $1/r^2$ loss associated with RF propagation through free space is a pivotal step for power and size limited RF systems.

OPTICAL FILAMENTATION

Self Channeling - Filamentation

In the early 1990s, as the field of ultrashort pulse laser research expanded, an increased interest developed in the propagation of ultrashort pulse lasers in gas, specifically in regards to the effect of the under-dense plasma created and how it affected focus (refs. 1 and 2). Under-dense plasma refers to the case where the wave frequency $\omega > \omega_{pe}$, the electron plasma frequency (ref. 3).

Building upon this research, Braun of the University of Michigan published a paper (ref. 4) entitled, “Self-channeling of high-peak-power femtosecond laser pulses in air.” In this paper, Braun and his team demonstrated for the first time (that we know of) the self-channeling, or self-focusing, of an ultrashort laser pulse over a distance of 20 m in air. This channel or “filament” as Braun described it, was a result of the “balance between self-focusing from the intensity-dependant refractive index and the combined effects of natural diffraction and refraction from the plasma created by the intense laser pulse.” His team was able to characterize this phenomenon over a laboratory scale distance and observed that the channel energy, diameter, and modulated spectrum all remained relatively constant with range. Braun’s team had in effect created a stable, ionized, and as demonstrated, a somewhat conductive pathway through the atmosphere. It was this experiment that opened the door for many applications, some of which will be discussed at the end of this section. For us, this filament presents a possible method to move off of the RF attenuation curve for free-space ($1/r^2$) propagation through the atmosphere. It

was attempted to take advantage of the conductive properties of the plasma and use it as a lossy wire surrogate. The degree to which filamentation will conduct RF energy will be mainly determined by the conductivity and lifetime of the channel, the dynamics of the channel itself, and also the ability to couple and transition RF onto the filament(s) themselves.

Phenomenology

Ultrashort pulse lasers, typically considered as lasers with pulse widths of less than a nanosecond, can convert modest wall plug power into very large peak power pulses by compressing the energy into a very small period of time. During propagation through the atmosphere, the ultrashort pulse wide bandwidth, optical pulses are affected by a phenomenon known as Kerr self-focusing. Kerr self-focusing causes the optical pulse to compress spatially as it travels through the atmosphere, continually increasing its peak intensity until it becomes so great that the pulse actually collapses resulting in plasma (ref. 5). Once the plasma is created, it serves to defocus the beam, which then begins to diverge. These two effects can actually achieve a balance with one another resulting in a stable plasma channel locked into a fixed diameter. As of yet, only an ultrafast laser, which can create pulses on the femtosecond time scale, can actually achieve a balance between these two phenomena resulting in what amounts to a continuous "string" of plasma through the air. This phenomenon is known as optical filamentation and serves as the conduit for our electromagnetic (EM) attachment.

Kerr Self-focusing

The optical Kerr effect was first observed in the early 1960s and is described as "nonresonant intensity dependant index of refraction" (ref. 6). The Kerr effect is a result of a medium's (in our case air) refractive index dependency. Specifically, the change in refractive index when subjected to large intensities of light. In this case (air), the steady state, unperturbed refractive index of a material or medium n becomes:

$$n = n_0 + n_2 I$$

Here, n_0 represents the linear component of the refractive index, n_2 represents the nonlinear component of the refractive index, and I corresponds to the intensity of the incident optical pulse. For the air and most other materials the nonlinear n_2 term is positive; therefore, a large intensity will result in a positive change in the index of refraction. In an ultrashort optical pulse, such as the one used for our research, the beam may, for example, have a Gaussian intensity profile with the largest intensities towards the center of the beam. The result of the Kerr effect on a beam such as this is a significant change in refractive index in the center portion of the beam profile. The higher effective index of refraction of the center of the beam in contrast with the refractive index of the outer portions of the beam actually creates a lens effect in the air. This lens effect, resulting from the Kerr effect, is the mechanism for the self-focusing of ultrashort pulses and is often also referred to as Kerr "lensing."

Now, in further detail, the self-focusing parameters of a Ti:Sapphire ultrafast laser system will be examined. Not only was there a concern with self-focusing of the output laser pulse as it propagates through the atmosphere, there was also a concern with self-focusing of the lower energy pulse in the laser amplifier as it was attempted to amplify it. This self-focusing must be taken into consideration when designing an amplification system based on Ti:Sapphire as the gain medium.

The critical power for self-focusing can be defined as (ref. 6)

$$P_{cr} = \frac{(1.22\lambda_p)^2 \pi}{32n_o \bar{n}_2}$$

This represents the minimum instantaneous peak power of a laser in order for self-focusing to occur. It can also be defined in terms of ω_{cr} , the critical size of beam fluctuations. It is possible for a beam to have a power higher than P_{cr} and not self-focus, if the beam fluctuations are very small. For example, in the case of a beam with a very smooth transverse beam profile, this relation can be used

$$P_{cr} = \frac{\pi \omega_{cr}^2}{2} I$$

Ultrashort pulse power levels for self-focusing were measured well above the conventionally known value for air of ~ 1.8 GW. This could be a result of the calculation methods used for determining \bar{n}_2 and their accuracy in the ultrashort regime (ref. 7). From P_{cr} , the self-focusing length L_{SF} can be defined, which cannot be exceeded regardless of beam profile

$$L_{SF} = \frac{0.5\rho_o}{\sqrt{\frac{P}{P_{cr}} - 1}}$$

Here, P represents the instantaneous power on axis of the Gaussian beam waist of the laser pulse of interest and ρ_o represents the Rayleigh range, defined as $\rho_o = n\pi\omega_o^2/\lambda_L$. The final equation necessary to define self-focusing for our system relates the pulse energy and spot size of the laser pulse. Assuming the amplifier is in saturation, the pulse energy $W = P\tau_p$, which is proportional to the saturation energy density, $\hbar\omega_L/2\sigma_{01}$ times the beam area A (where $A \sim \frac{\pi\omega_o^2}{2}$) can be defined.

For many of the experiments, laser pulse energy of ~ 100 mJ with a pulse width $\sim 100 \times 10^{-15}$ s or 100 fs was measured. This corresponds to an instantaneous peak power $P \sim 1 \times 10^{12}$ W or 1 TW. For a typical Ti, sapphire laser amplifier driven to saturation operating at a wavelength near 800 nm, the self-focusing length L_{SF} is on the order of a few centimeters. In the next section, the operation of the ultrafast laser system itself was examined in more detail and self-focusing as it relates to chirped pulse amplification (CPA) was more closely looked at.

Propagation through the Atmosphere

As described previously, the extremely short, high intensity pulses created by the laser system interacts with the air via the Kerr effect resulting in spatial self-focusing of the pulses. The resulting collapse of the pulses that ensues creates a region of plasma. This alone could be a useful state for some applications; however, in this case, there was a need to balance out this self-focusing effect in order to effectively 'stretch out' this plasma. Under the proper conditions, the plasma itself defocuses the beam and opposes the self-focusing with little loss of energy. The balance of these two effects and corresponding focusing and defocusing (fig. 1) results in a continuous extended region of plasma that creates a filament.

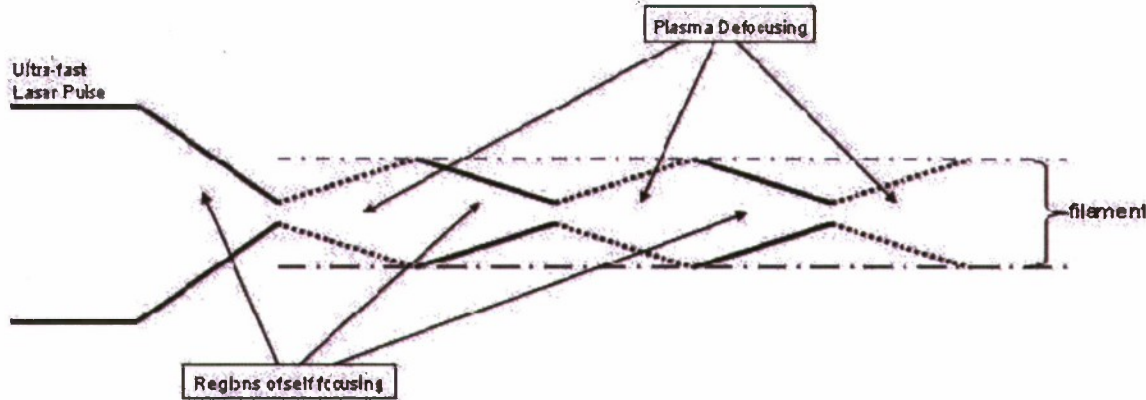


Figure 1
Filament formation

The main mechanism responsible for the creation of this plasma is multiphoton ionization. Multiphoton ionization occurs when an atom absorbs multiple photons, each with energy $\hbar\omega$, resulting in a combined photon energy $n\hbar\omega$ sufficient enough to knock an electron free of an atom. The multiphoton ionization rate based upon perturbation theory is given by (ref. 8)

$$\Gamma_n = \sigma_n I_L^n$$

where I_L^n represents the intensity that is dependent on the number n of photons, and σ_n is the cross-section. Prior to the discovery of the laser, it was believed that a single photon with energy $\hbar\omega$ was only capable of ionizing an atom if $\hbar\omega$ was greater than the electron binding energy as predicted by the photoelectric effect. With the development of the laser in the 1960s, it became possible to achieve much higher light intensities than was previously possible and experimental multiphoton ionization was observed.

Referring back to figure 1, the n_2 term in the nonlinear refractive index equation for air may account for the Kerr self-lensing effect and resulting focusing of the laser pulse; however, let's examine more closely the counter-balancing effect of the low-density plasma that results from this focusing. The change in the refractive index of the air as a result of the plasma can be described as $-\omega_p/2\omega^2$ (ref. 4); where the plasma frequency $\omega_p = \left[\frac{4\pi e^2 n_e(I)}{m_e} \right]^{\frac{1}{2}}$, m_e is the mass of the electron, ω is the optical frequency, and $n_e(I)$ represents the intensity-dependant plasma density. When filamentation occurs, this negative change in refractive index in conjunction with the positive n_2 index of air can lead to a stable ionizing pulse that is capable of traveling in this state for several meters. For a Ti:Sapphire laser system, similar to the one that will be used to conduct our experiments, operating at $\lambda=775$ nm, Braun calculated a plasma density of $4.5 \times 10^{16} \text{ cm}^{-3}$ required to balance the self-focusing with an optical intensity of $7 \times 10^{13} \text{ W/cm}^{13}$.

Since the air chemistry and physics involved in the process of filamentation were both briefly discussed, some of the possible applications of this phenomenon can now be discussed, in general, before digging deeper into the case of the RF/plasma filament interaction which is the focus of this report.

ULTRAFAST LASERS

Broad Band is Ultrashort

There is a definite relationship between the frequency bandwidth to the pulse width of a pulsed laser. This relationship can be exploited (as described in the next section) in order to amplify ultrashort laser pulses.

The relationship can be described as follows (ref. 13)

$$\Delta t \omega \geq \frac{1}{2}$$

where Δt represents the pulse width of the pulsed laser and $\Delta \omega$ represents the frequency bandwidth of the pulse. It then becomes obvious that the smaller the pulse width of the laser source, the larger the bandwidth will become in order to obey this relationship. Looking at the parameters of our system as an example, a 100 femtosecond laser pulse would require a minimum bandwidth of close to 11 nm. This minimum value, however, can only be reached for a Gaussian-shaped pulse. A pulse with $\Delta t \Delta \omega = 1/2$ is said to be transform limited. A transform limited pulse will propagate through the atmosphere with a constant pulse width (aside from dispersion effects). In some cases, a pulse is not transform limited and its instantaneous angular frequency varies with time. What results is known as a "chirped" pulse. For a chirped pulse, the instantaneous frequency of the pulse may be "red shifted" or "blue shifted." This means that the pulse may have more red or blue (where red represents longer wavelengths and blue represents shorter wavelengths of light) frequency components on either the front or back end of the pulse. The result of this inhomogeneous spectrum is evident as the pulse propagates through the atmosphere. Red and blue frequencies travel at slightly different velocities in air due to the wavelength dependence of their refractive index dependant velocities in the air. If the leading edge of a laser pulse is traveling more slowly than the trailing edge, the trailing edge will eventually catch-up to the leading edge; resulting in pulse compression. This chirp effect is taken advantage of in order to amplify ultrashort laser pulses.

Chirped Pulse Amplification

In order to create the optical filaments used for the interaction with EM waves, an ultrashort pulse laser system based upon CPA was used. Chirped pulse amplification involves taking an ultrashort pulse, in our case one with a pulse width <50 fs and a spectral width of >15 nm, and an output energy of >1.7 nJ and stretching this pulse. If the pulse was not stretched, the self-focusing of the ultrafast beam described in the previously section would occur inside the laser amplifier possibly resulting in breakdown, limiting amplification and damaging optics. For the highest efficiency in the system, the Ti:Sapphire crystal needs to be pumped at close to saturation, but doing so with very short pulses and very large bandwidths would result in thermal

damage to the optical components in the amplifier. Without the use of CPA, the stretching is performed via a number of reflections off of a pulse compression grating. Compression gratings for this application are typically manufactured using holographic techniques and use a unique gold coating for high diffraction efficiency as well as a high damage threshold (ref. 14). In figure 2a, the seed beam is shown making multiple reflections off of the grating in order to achieve a positive dispersive delay.

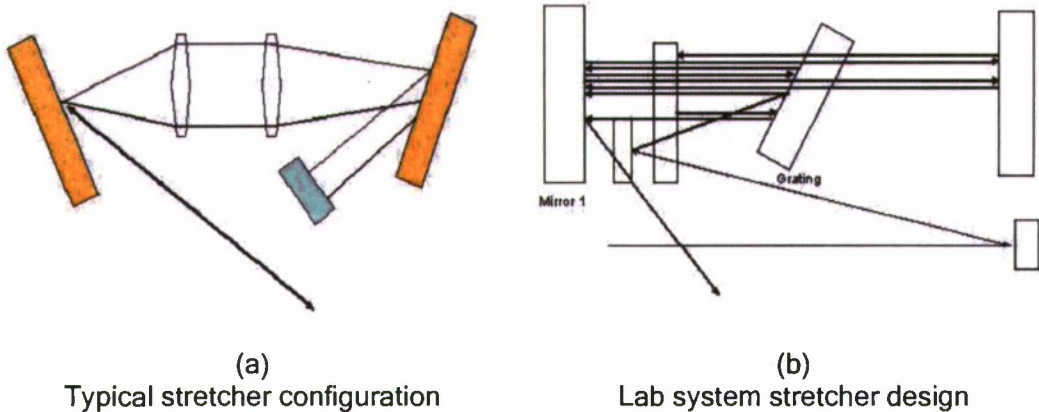


Figure 2
Pulse compression grating

The figure shows a straightforward view of how the compression scheme works; however, due to space limitations in a typical ultrafast laser system, beams usually make multiple reflections off the gratings resembling more closely figure 2b, as in our system. The principle is that two parallel beams of different wavelengths (various spectral components of the seed beam) will remain parallel after reflections off the grating, however, will have traveled different distances allowing for a tailored stretching or as we will be seen, compression of the optical pulse in time. Multiple passes are made to increase the dispersion as well as to arrange the wavelength components collinearly. Figure 3 shows the stretcher configuration in our laser system that will be used for our experiments.



Figure 3
Lab system compressor beam path

Although the exact location of each pulse may be difficult to discern from this picture, it gives a feel for the number of passes that are made off of a single diffraction grating in order to achieve the desired stretching delay. This stretching is necessary not only to protect the optics but also to prevent damage to the optical crystal itself due to the extremely high peak powers that would result from amplification of a femtosecond pulse.

Once the pulse is stretched it continues on to the regenerative amplifier (fig. 4). The laser gain medium of this amplifier is Ti:Sapphire as mentioned earlier. The stretched pulse makes multiple passes through the Ti:Sapphire crystal, which is pumped by roughly 10 mJ of energy from a frequency doubled Nd:YAG pulsed laser source operating at 532 nm. A cavity is created using thin film polarizers in conjunction with a Pockels Cell. The Pockels Cell allows the pulse (which is monitored by a photodiode behind the end cavity mirror) to be contained, releasing it when the maximum energy is obtained by changing the applied voltage to the crystal medium in order to rotate the polarization resulting in a pass rather than a reflection off of the thin film polarizer. After being released from the regenerative amplification cavity, the output energy of the pulse is ~1.5 mJ.

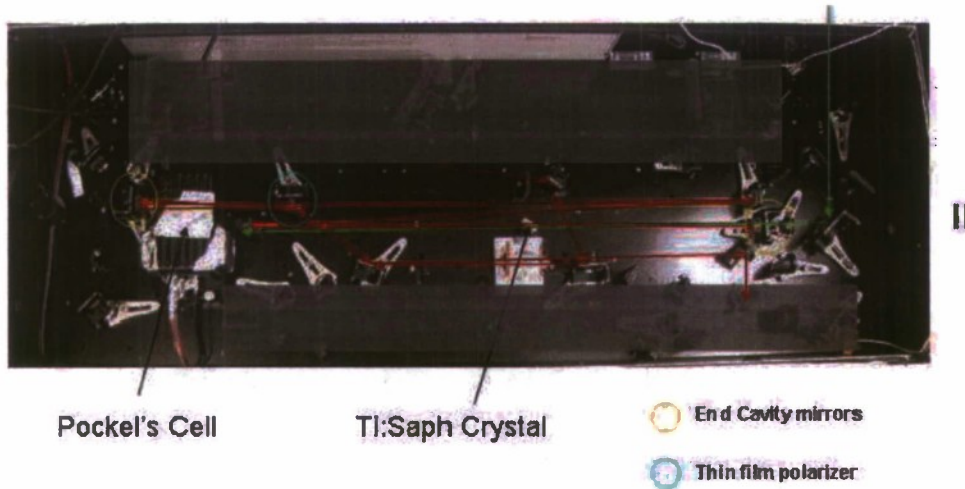


Figure 4
Regenerative amplifier

The stretched, and now amplified pulse, then continues on to a second amplification stage known as a multi-pass or "bow-tie" style amplifier. This amplifier also relies on Ti:Sapphire as the gain medium and is pumped with 90 mJ from the same Nd:YAG source that was split with a 90/10 beam splitter in order to pump both cavities simultaneously. In the multi-pass amplifier, the stretched pulse will make four passes through the Ti:Sapphire crystal, the cumulative gain results in a pulse of ~19 mJ (fig. 5).

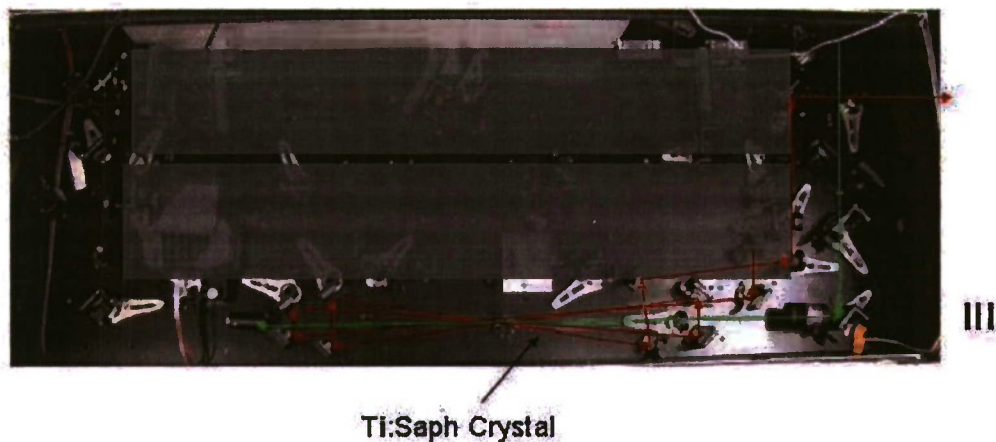


Figure 5
Multi-pass amplifier

A third amplification stage was added to the system in order to achieve higher energy and more significant filamentation. This stage is yet another Ti:Sapphire multi-pass type amplifier (fig. 6); however, this crystal is much larger in diameter and length and is pumped by nearly 1 J from a higher energy Nd:YAG doubled pump source. The result is a stretched pulse with an energy >150 mJ, which is then sent through a compressor in order to restore it to close to the original pulse width of the seed laser. The compressor works by the same principle as the stretcher, but in reverse. Multiple reflections are made off of a pair of gratings in this case; resulting in a negative dispersive delay to compensate for the positive dispersive delay, or chirp, from the stretcher.

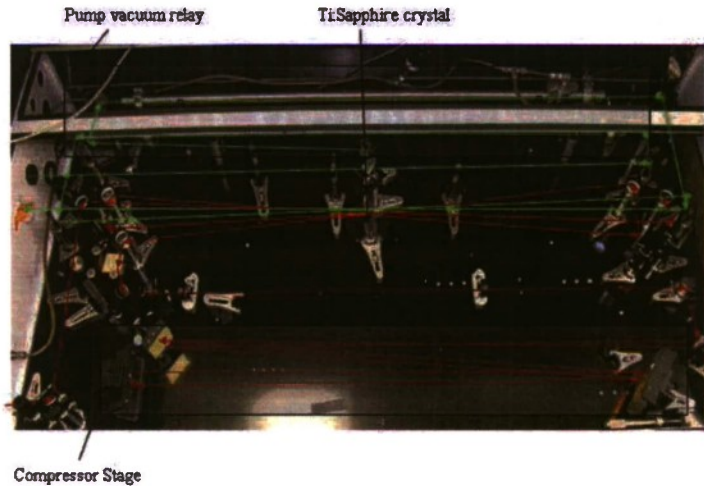


Figure 6
TW amplifier

Peak Powers, Intensities

The CPA scheme described allows for large gain amplification of very short optical pulses. The result is peak power levels on the order of TW; in our particular setup, ~ 1 TW (~ 100 mJ per pulse). This is even more significant considering the very modest wall plug power requirements, but understandable since the average power levels of the system are very low ~ 1 W! It is these very short, very intense optical pulses that are required in order to create

filaments in the air. With an output beam diameter of ~15 mm, our laser beam will form filaments if left to propagate freely through the atmosphere due to Kerr self focusing (as described in the previous section) after a few meters. However, in our experiments, due to space limitation, using a plano-convex lens or Galilean telescope configuration to focus the beam in addition to fine tuning the compressor length for chirp control in order to create filaments in space where needed. Average filament diameters were measured to be roughly 100 μm although, depending on the energy of the optical pulse, bundles of many optical plasma filaments in one beam were observed (ref. 15). At energies over 20 mJ it is very common for multiple filaments to form due to spatial inhomogeneities in the beam profile. However, it is possible to form a single filament at this level with a spatial beam profile that is fairly homogeneous. At power levels above the range of 20 to 30 mJ, without additional beam conditioning multiple filaments are observed. Energy levels of individual filaments were measured to be ~2 mJ with intensities on the order of 10^{13} to 10^{14} W/cm^2 .

FILAMENT INTERACTION WITH ELECTROMAGNETIC WAVES

Filament Conductivity

For the purposes of our research, the modeling and simulation theoretical studies were performed under the assumption that the plasma filament can be represented as a plasma "wire." In reality the conductivity of a filament created by an ultrashort laser pulse in orders of magnitude is less than that of a wire or perfect electrical conductor (PEC). Ladouceur et.al of NRL calculated the conductivity of an optical filament created by a self guiding TW laser pulse over a 200 ns time scale using a non-linear low inductance circuit model of their experiment (ref. 16). Over the 200 ns time frame, the resistance ranged from an initial value of $3.6 \times 10^5 \Omega\text{m}^{-1}$ to a final value of $6.4 \times 10^7 \Omega\text{m}^{-1}$ at 150 ns. They also determined that these calculated values are linearly dependent upon the value of the collision frequency. If we take, for example, the best case resistance of the filament at $3.6 \times 10^5 \Omega\text{m}^{-1}$ (the initial value) and compare it to the resistance at 20°C of a 20 AWG copper wire $\sim 0.0323 \Omega\text{m}^{-1}$, it becomes obvious that there are some major differences to consider. $3.6 \times 10^5 \Omega\text{m}^{-1}$, however, is still a significant improvement over air which is estimated between 10^{13} - $10^{15} \Omega\text{m}^{-1}$ depending on altitude and atmospheric conditions.

Radio Frequency Interaction

Let's begin the discussion now of the EM radiation in the form of the RF waves, which was attempted to attach to the laser generated filaments. Radio frequency radiation in waveguide and propagating from antennas such as those used in our experiments can occur in a variety of modes or waves. These refer to the orientation of the electric and magnetic components of the field as it propagates either through free space or in waveguides or transmission lines. In general, they can be group them into three main categories, transverse electromagnetic (TEM) waves, transverse electric (TE), and transverse magnetic (TM) modes.

Transverse electromagnetic waves can be supported in systems comprised of two or more conductors. A simple example of TEM wave propagation would be twin wire cable where two wires are oriented parallel to one another and insulated from one another to maintain a calculated separation. The TEM waves also represent plane waves, these waves will be emitted from our transmission antennas once in the far field zone and considered for modeling of such situations. In the case of plane waves, the conductors are considered to be infinitely large plates spaced infinitely apart from one another (ref. 17). In this case there is no longitudinal component of either the electric or magnetic field, both of which are in the transverse direction.

Transverse electric waves describe waves with their magnetic field in the longitudinal direction and without electric field in the longitudinal or in the case of waveguide, axial direction. The TE modes can propagate in waveguide and represent the dominant mode in rectangular waveguide, specifically the TE_{10} mode. A series of tests with a pair of wires serving as filament surrogates that were oriented perpendicular to the face of an open ended waveguide in order to excite an electric field in the direction of the wires were conducted. In this scenario, the TE mode created in the waveguide to direct the radiation along the axis of the wires was taken advantage of.

Transverse magnetic waves represent waves where the electric field component of the field is directed longitudinally and there is no magnetic field in this direction. Although TM modes may or may not be (depending on the geometry of the waveguide) the dominant mode in cylindrical waveguide, they propagate more efficiently in circular waveguide as opposed to rectangular waveguide. It is for this reason that the circular waveguide was chosen to construct our resonant cavity that is detailed later in this report. By carefully selecting the dimensions of the circular waveguide as well as the length of the waveguide between two end caps, it was possible to resonant a TM mode inside the cavity. This allowed the set up of a very strong electric field in the direction of a filament propagating through the cavity with a much lower RF drive power. This orientation and cavity setup was used for a number of applications in physics, including RF electron guns (ref. 18). In this case, the electron source will be replaced by an aperture through which the laser will propagate.

One of the primary challenges faced when attempting to efficiently attach RF to a plasma channel is determining which mode is ideal. This also will change and depend on the particular orientation of the filament or filaments and the coupling technique proposed. In this regard, various types of waves will be examined in this report in an attempt to optimize laser filament/RF interaction.

Ultrafast Laser Filament/ Radio Frequency Interaction

In order to determine the optimum RF attachment to our plasma filaments, coupling of various modes of RF to filaments positioned in different orientations will be examined. For TE mode coupling as discussed previously, it is wished to orient the electric field along the direction of the plasma wire. One method of accomplishing this would be to use a rectangular waveguide open at one end. The plasma filament would be oriented to travel across the face of the open ended wave guide in order for the electric field lines to point in the same direction as the filament axis. Also it was discussed using a circular resonant cavity designed to resonate a specific frequency of RF. Such a cavity can be designed so that the electric field is pointing towards the flat face of the cylinder. It would then be possible to send a plasma filament directly though the two end faces such that the electric field is oriented along the filament. It may also be possible to run multiple wires or filaments along the outside case of a section of waveguide in order to transfer the field from the waveguide on to the filaments. Finally, the case of a plane wave propagating from a common horn antenna coupling onto a pair of filaments, which in effect makeup a two-wire transmission line could be looked at.

EXPERIMENTAL SETUP

This section will detail the equipment used in the experimentation.

Lasers

For the in house laboratory experimentation, a CPA laser system was used as follows:

Pump Lasers -

- Spectra-Physics "Quanta-Ray" Lab-190-100 Nd:YAG Lab Series Pulsed Laser
Specifications: Energy per pulse at 532 nm >100 mJ, 10 Hz reprise
- Continuum "Powerlite Precision II" Model # PR-9010 Nd:YAG Pulsed Laser
Specifications: Energy per pulse at 532 nm ~ 1000 mJ, 10 Hz reprise, pulse width at 532 nm ~ 4-8 ns, beam pointing stability +/- 30 μ rad, beam divergence ~0.45 mrad, and energy stability ~3%

Oscillator -

- Femtolasers "Integral 50"
Specifications: pulse width < 50 fs, spectral width > 15 nm, output power > 100 mW, output energy @ 85 MHz > 1.7 nJ, and wavelength ~800 nm

Optical Amplifiers -

- Originally designed by Quantronix Corp. Modified to provide better stability and reliability (discussed in an earlier section)
Multi-pass amplifier output ~19 mJ, 10 Hz, pulse width 200 to 250 ps

Radio Frequency Sources

- Amplifier Research "1000W1000C" Solid State Linear Amplifier (fig. 7)
Specifications: 1000 W minimum output power, frequency response 80 to 1000 MHz, input impedance 50 ohm, and VSWR 2.0:1 maximum. Capable of continuous wave (CW) output pulses

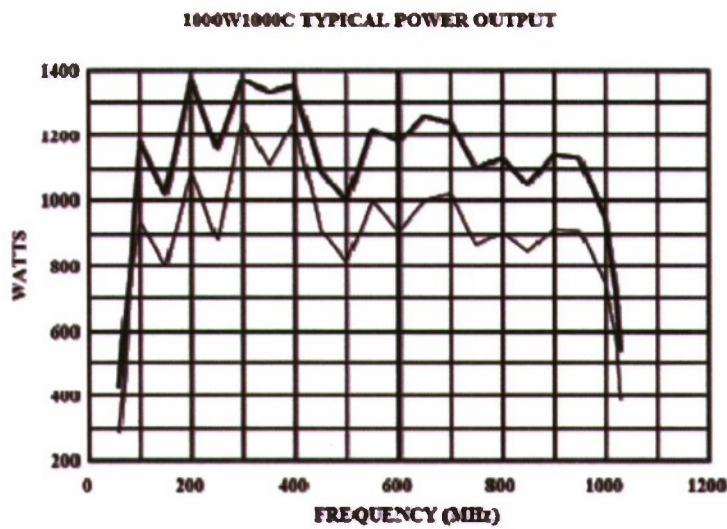


Figure 7
RF linear amplifier gain plot

- D.E. Technologies TWT RF source
Specifications: Power > 2 kW, pulse width > 6 μ s
- Hewlett Packard 8643A Synthesized Signal Generator
- Agilent E4433B ESG-D Series Signal Generator
- BNC Module 500 Pulse Generator
- HP 8350B Sweep Oscillaotor

Detection and Measurement Equipment

- Tektronix RSA 3408A Real-Time Spectrum Analyzer
- Prodyn DDot
- Horns
- Tektronix TDS 6604 Digital Storage Oscilloscope
Specifications: 6 GHz, 20 GS/s
- Grenoule ultrafast laser measurement device
- Ocean Optics HR2000CG-UV-NIR High Resolution Spectrometer
- Gentec Laser Energy Detector
 - Head - QE25LP-S-MB

Specifications: Spectral range 0.19 to 20 μm , typical sensitivity 10 V/J,
Maximum pulse energy @ 1.064 μm ~3.75 J

- Optical Diffuser
- Meter - Gentec Solo-PE

EXPERIMENTS

Single Wire Propagation (Copper)

The investigation of the mechanism for coupling of the TE_{10} mode for an ideal scenario using a copper wire as a surrogate for our plasma filament was begun. Beginning experiments with copper wire as a surrogate makes measurement an easier task, for the wire is continuously present (as opposed to the short lifetime of the plasma filament) and its conductivity is much higher than for the case of the plasma. The free electron number density for copper is on the order of $8.5 \times 10^{28} \text{ m}^{-3}$ or $8.5 \times 10^{22} \text{ cm}^{-3}$ (ref. 19). As will be demonstrated later in the section on theory and modeling, the coupling efficiency and conductivity of the plasma channel with regards to RF increases as a function of increasing electron density. This is intuitive since a higher electron density translates to a higher number of electrons per volume, which increases conduction of electric field through the wire.

For this test, it will begin by using an open ended waveguide section fixed with a waveguide to coax adapter with a type-N connector as the feed point for RF. As shown in figure 8, the face of the open-ended waveguide is oriented perpendicular to the axis of the wire.

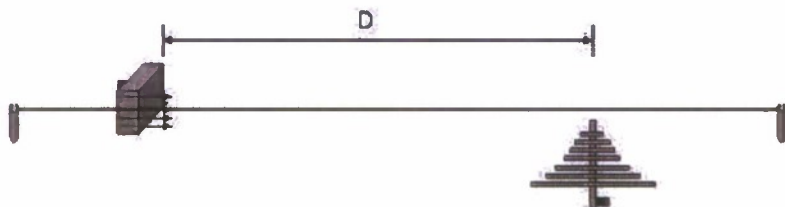


Figure 8
Single wire (copper) propagation layout

The waveguide used in this case is WR-284 rectangular waveguide driven such that the dominant mode is TE_{10} . The direction of the electric field for this TE_{10} mode is pointed in the same direction in which the RF cable enters the waveguide to coax adapter. In this orientation, the electric field will point along the direction of the wire axis. The wire is 0.8 mm copper wire, fixed at both ends and insulated at both ends to prevent electrical contact with either the fixture or the table. The open ended waveguide is driven with the Agilent E4433B ESG-D Series Signal Generator, which can generate a signal of up to ~16 dBm (frequency dependant) and operates over a frequency range of 250 kHz to 4.0 GHz. Due to the supported wavelengths of the WR-284 waveguide, this test will be operated over the frequency range of ~2.2 to 3.5 GHz. To measure the extent of coupling along the copper wire, a Log Periodic (L.P.) type receive antenna was used, manufactured by A.H. Systems, model SAS-515; oriented with its feed in the direction of the electric field (along the axis of the wire). The distance (D) between the receive antenna and the open-ended waveguide was varied in order to measure power received along the wire as a function of distance. The output of the L.P. antenna was analyzed on the Tektronix

RSA 3408A and power measurements were recorded at specific frequencies. The measurements were then repeated again, this time with the wire removed in order to determine the change in RF power at specific locations. A decrease in RF power with the wire present, represented possible absorption of reflection of the RF field by the wire; whereas, an increase in power represented an attachment of RF to the wire and subsequent propagation enhancement. In this experiment, RF power levels are being compared with and without the wire present in the field; therefore, the only concern is with relative power levels and not with losses from cables, connectors, etc at this time. The environment has many reflective surfaces and is in no way anechoic, so such a baseline measurement at each distance was useful to help account for interference from reflections off the walls, objects in the room, the floor, etc.

Figure 9 shows the received RF power versus distance for the case of the single copper wire and the same scenario without a wire. The trend for the non-wire power measurements are as would be expected, falling off over distance. However, for the case with the copper wire present, after the initial coupling loss the copper wire power remains close to constant over distance. This result was consistent with low loss transmission of RF, or in other words, the wire in this case acted as an effective transmission line over this distance.

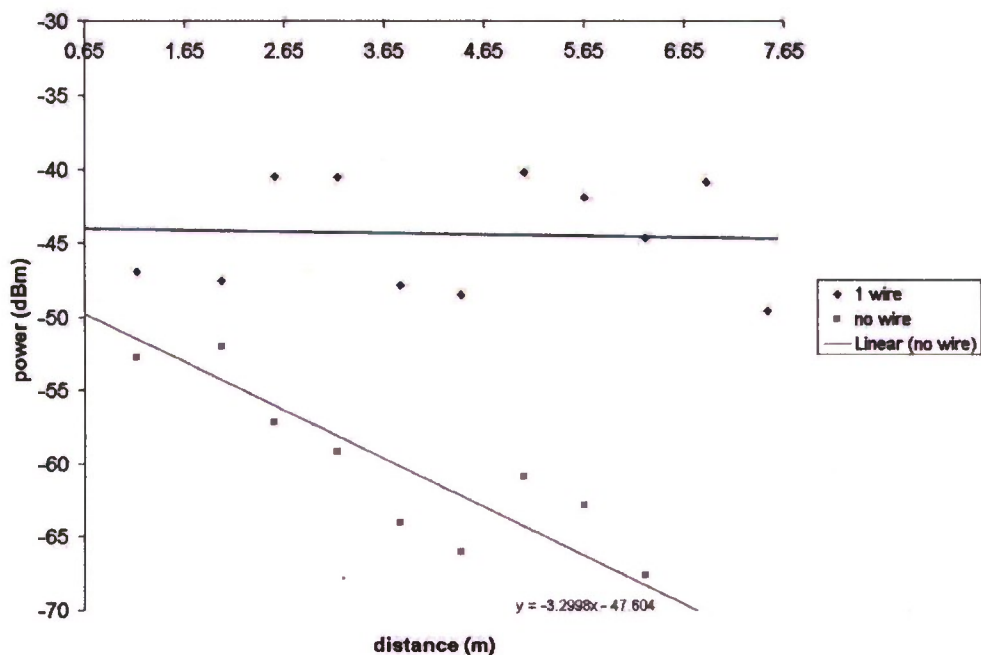


Figure 9
Single copper wire propagation

The single wire data was then normalized by subtracting out the free space data at each respective measurement distance from the source in order to look for change in RF power as a result of the copper wire versus the distance from the source (fig. 10).

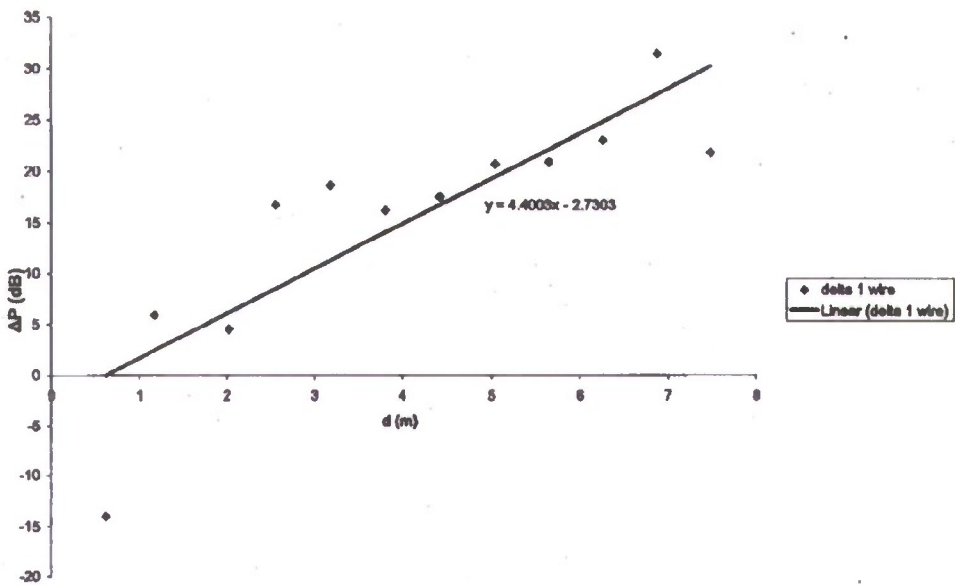


Figure 10
Normalized single copper wire propagation

Figure 10 demonstrates an increase in the advantage of copper wire attachment versus free space propagation as the distance from the source increases. There was an initial decrease in RF power with the copper wire present very close to the antenna, possibly due to the geometry of the optical table and mounting equipment close to the open-ended waveguide location. In this orientation, only side-lobes were present and the antenna blocked much of the radiation from reaching the antenna. The positive slope of this normalized power curve would be expected, for as the field drops off naturally in space, it continues to propagate on with much lower loss when using the copper wire as a conduit.

Similar trends are expected in future high power RF and plasma filament experiments. Due to the much lower electron density of the plasma filament in contrast with the copper wire however, the extent of the coupling power advantage is expected to be significantly reduced.

Two Wire Propagation

For this experiment, it was intended to characterize the coupling of the TEM mode along two copper wires as surrogates for plasma filaments. The setup for these tests used two standard gain horns, one as a transmitter, the other a receiver oriented at different angles with respect to the wire(s). The wire was standard bare copper wire, 0.8 mm in diameter (~20 gauge), in this case a pair of copper wires, where the spacing and orientation was varied to determine coupling dependence on wire geometry and position.

Figure 11 plots received power, normalized to free space without wires versus distance from the transit horn. Notice when the data points are fitted with a linear fit, a trend of increasing power as was seen in the case of the single copper wire was observed. In this case, there was a significantly higher slope for the case of wire spacing 2λ versus for λ spacing. In the next section on the modeling for this experiment, this result is predicted theoretically. Also predicted was a higher slope for the case of two-wire propagation when compared to the single wire case discussed in the previous section. This may have resulted from the coupling efficiency from the RF horn to the wire pair. It was observed that coupling was highly dependent on spatial

orientation and angle of incidence. Due to lab constraints, it was questionable whether it was possible to get into the far field (required for a clean TEM transmission mode). Therefore, near field effects may have played a part in this lower than expected slope. Experimental factors were most likely to blame. Wires tended to sag and it was difficult to keep them parallel to one another over the entire distance. Two wire transmission lines as studied by Goubau in the late 1950s are very dependent on position with respect to one another (ref. 20) which could explain lower than expected improvement in this case. In the future, the dependence on coupling to a 2-wire set on angle of incidence and distance as well will be investigated.

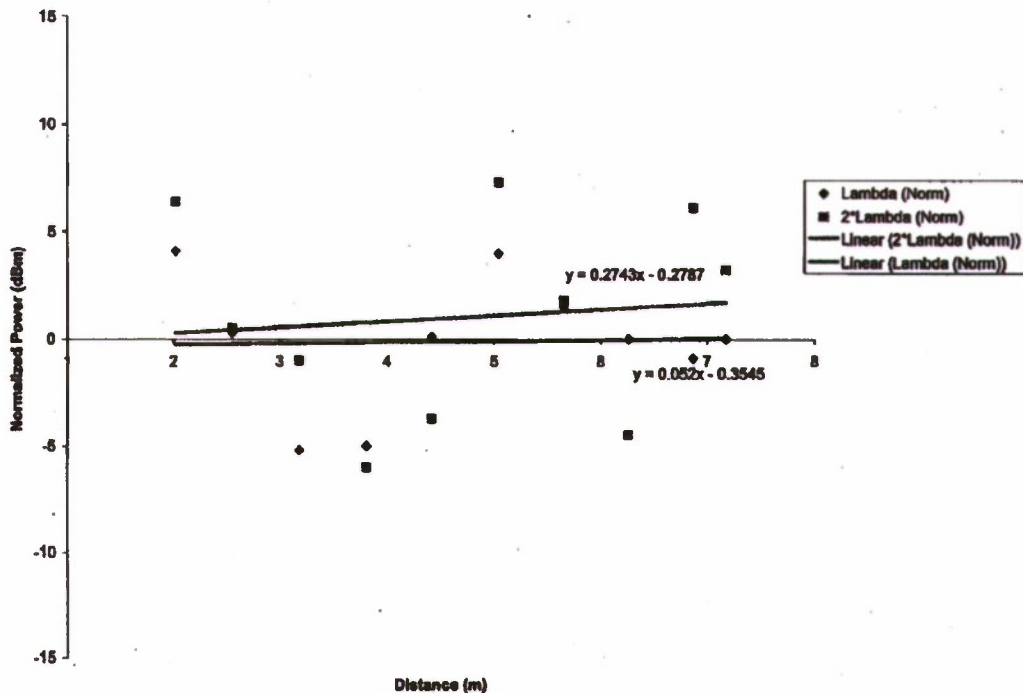


Figure 11
Dual copper wire RF propagation

When optimized, theory predicts that attenuation will be lower for RF transmission down a pair of filaments at a spacing of 2λ . With sufficient laser energy, it would be possible to split a beam into two, thus creating two plasma filaments in order to take advantage of TEM coupling from a horn antenna. After splitting losses the energy of our current laser system is not sufficient for this mode of coupling; however, it is planned to investigate this further in the future.

Rectangular Waveguide Interaction

In order to determine if RF attachment to plasma filaments is feasible, it must first be demonstrated that the two do in fact interact and that to capture this interaction is possible. The initial proof of principle experiment conducted with actual plasma generated by an ultrashort pulsed laser was designed to characterize interaction (if present) of a small plasma filament inside a rectangular waveguide driven by an RF amplifier. The waveguide cavity enables us to monitor a uniform standing wave without issues related to wave reflection and interference. If such an interaction were present it would represent the potential for plasma to have an impact on an EM field in some form; i.e., reflection, absorption, etc. This experiment was the starting point for the study of RF/plasma interaction and eventually RF/filament interaction.

The setup was as follows (fig. 12) and used a specially adapted rectangular waveguide system that enabled us to setup a standing wave at a desired frequency and amplitude with which the characteristics in a controlled environment could then be measured. Attached to one end of a straight section of WR-284 waveguide was a waveguide to coax adapter where an RF signal was fed. On the opposite end of the straight waveguide section a similar waveguide to coax adapter was connected to an oscilloscope in order to analyze the throughput signal, in some cases an input coupler was used in order to measure back reflections through the cavity. The RF throughput signal for any perturbations in the signal coinciding in time with entrance of the laser pulse was observed. The direction of the electric field for the waveguide was in the axial direction along the direction of laser propagation. The laser pulse timing was monitored via a silicon photodetector placed behind one of the directional mirrors capturing the leakage light, converting this light to voltage that was monitored on the oscilloscope. A hole was drilled through the center of the waveguide straight and two waveguide below cutoff (WBC) cylindrical filters 6.25-mm inner diameter and ~25-mm long, one on each side. These filters allowed the laser to propagate through the chamber but limited leakage of RF from the waveguide itself.

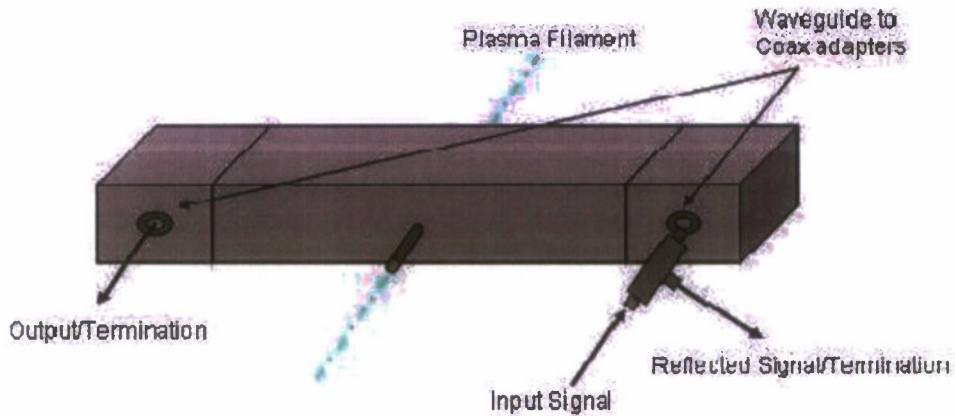


Figure 12
Rectangular waveguide fixture

A laser pulse of ~60 mJ and ~100 fm-sec, was sent through a positive focal lens ($f \sim 125$ mm) in order to form an intense, visible short plasma filament. The lens was positioned such that the highest intensity segment of the plasma filament passed through the WBC and was centered inside the waveguide.

In order to gauge the sensitivity and operation of the experimental setup, a copper wire was inserted through the waveguide fixture while feeding a CW signal and monitoring the transmission. Upon insertion of the copper wire, the field inside the cavity was disrupted substantially, proving the concept for the case of PEC.

Returning to the case of laser generated plasma, figure 13 shows its interaction with the EM field inside the waveguide cavity. The RF signal in this case was ~2.6 GHz and the sensitivity of the setup allowed the system to be driven with very lower power (<10 dBm) in order to look for subtle field perturbations. The interaction presented itself in the form of an increase in RF signal transmitted following the input of the laser pulse as observed by the photodiode signal.

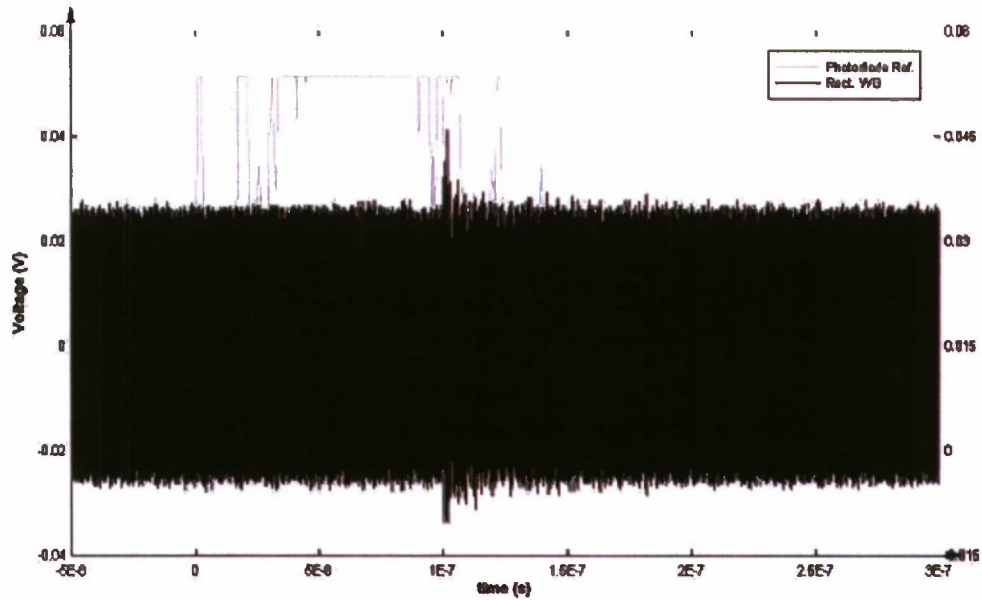


Figure 13
Rectangular waveguide interaction

The observation of this disturbance in the EM field due to the plasma filament is a positive indication that the electron density and lifetime of the plasma filament may be sufficient under certain conditions to carry RF energy. However, the extent of interaction in this scenario is minimal, a blip above the noise floor. Thus, in order to enhance this interaction, it is necessary to increase our RF or laser energy and subsequently the electron density of the plasma filament. Unfortunately, with the current laser system available, increasing the laser energy is not an option, therefore, the follow-on experiments deal with methods of increasing the RF field strength for potential plasma enhancement.

Resonant Cavity Interaction

The rectangular waveguide experiments demonstrated that either a higher laser energy or high RF power level would be required in order to see an interaction between the plasma filament and RF fields. The laser energy cannot be increased at this time, so a cylindrical RF cavity [as discussed in most EM textbooks (ref. 20)] was used to achieve the field strengths required and to increase the electron density of our plasma filament(s) without the need for large very high power RF sources. Electrical breakdown and plasma formation in the air caused by very high RF field strengths was demonstrated and thoroughly investigated (ref. 22). It would, therefore, be plausible that a sufficient RF field would enhance existing plasma and could potentially significantly increase the electron density of the plasma channel. As mentioned earlier, a higher electron density should translate to a high conductivity and thus a greater interaction between the RF field and plasma channel. This brings us a step closer towards our goal of RF attachment.

In this series of experiments, the coupling of RF energy to a plasma filament taking advantage of the very high field intensities created in the circular resonant cavity was examined. In this setup, we propagate a 100 fs, 100 mJ laser pulse (10 Hz) through an aperture in the center of a circular cavity to determine the extent of interaction and whether it was possible to couple RF energy to the outside. This setup also allowed the determination of whether the filament would conduct energy out of the chamber. The experiment was repeated with two

cavities, each designed for a particular frequency in order to evaluate the relationship, if any, between RF frequency and extent of coupling to a single filament and also served as a general comparison of trends. The filament or bundle of filaments was created with a focal lens ~4 m from the compressor stage in order to achieve filaments within the range of our laboratory.

900 MHZ Resonant Cavity

The first cavity (which will be referred to as cavity A) was designed with a center frequency of ~900 MHz and constructed out of aluminum tubing with flanged end pieces that could be removed, but also provided enough surface contact to ensure a high quality (Q) factor for the cavity (fig. 14).

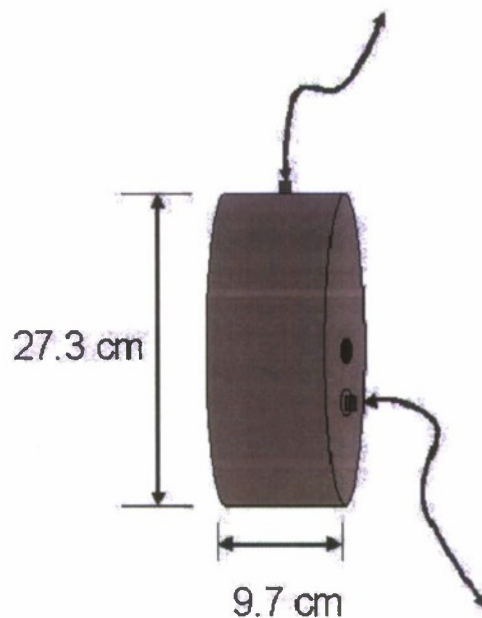


Figure 14
Cylindrical resonant cavity (cavity A)

This cavity creates a TM_{010} dominant mode with the electric field pointing in the axial direction, or along the filament as was the case for the rectangular waveguide experiment detailed in the previous section. This mode allows for a longer length of interaction with the filament and a more efficient delivery of the RF energy available. The cavity was fed from the side wall and a small probe was mounted on the front wall in order to monitor the electric field buildup and decay inside the cavity. The feed for the cavity was mounted to a small magnetic dipole that was grounded to its base and adjusted for the highest possible Q value. After a few design iterations it became apparent that the Q for the cavity was highly dependent on the contact between the body and end faces of the resonator in addition to the size and positioning of the magnetic dipole loop. The end face probe was a very short stub attached to a type N-connector for output to an oscilloscope or analyzer. In order to extract accurate electric field numbers, it would be necessary to calibrate this stub in order to calculate its effective area. Unfortunately, the resources were not available to do so accurately. Therefore, for this test, the cavity probe serves as a relative indicator of cavity activity. For this cavity, a Q of ~7150 measured via a S12 on a network analyzer was achieved and calculated by $\omega_o/\Delta\omega$, where ω_o represents the center frequency and $\Delta\omega$ the bandwidth at full width half maximum (FWHM) (fig. 15).

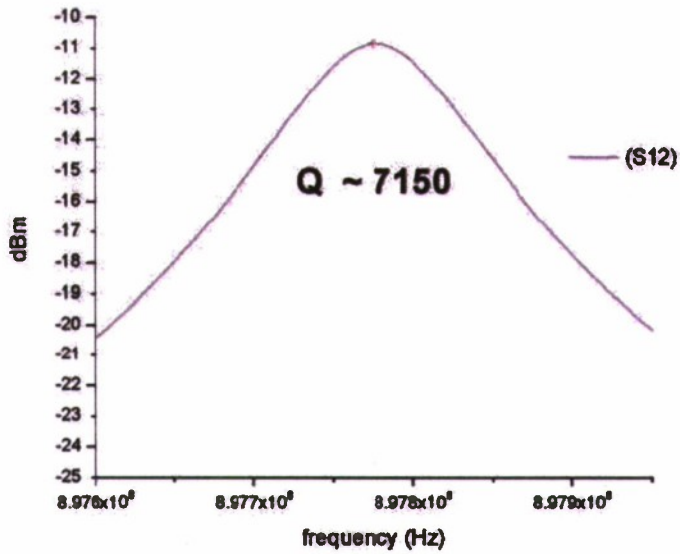


Figure 15
Q, cavity A

The cavity was fed by a linear RF amplifier delivering greater than 1000 W of RF power and capable of operating continuously. In this experiment, the RF amplifier was driven with a low power RF signal generator trigger by a pulse generator that was synchronized with the pump laser in order to deliver ~ 10 μ s pulses in time with the laser pulses. A photodetector was also placed downstream near the laser aperture in order to provide a relative reference estimate of the laser pulse in time with respect to the RF pulse when viewed on an oscilloscope in order to sync the RF and laser pulses in time. A D-dot sensor, which measures the derivative of the electric field, was placed a few inches behind the resonant cavity allowing the filament to pass by its edge. This allowed any attachment and delivery of RF outside of the cavity to be monitored.

Initially, a plano-convex lens with a short focal length (125 mm) was used in order to create a visible spark of plasma that could center on the hole through which our laser would exit the cavity. This insured that a conduction path from the inside of the cavity to free space was made. The sharp focus created a visible plasma spark ~ 10 mm long, not the long filaments that have been discussed, however, it allowed us to start with a high electron density to compensate for the limited laser energy in order to prove the principle of conduction and attachment.

The laser pulse was then fed into the cavity and using the photodiode signal as a reference, the pulse was centered in time relative to the RF pulse so that interaction occurred for the entire lifetime of the filament or plasma created. Figure 16 demonstrates the interaction observed when the laser was fed into the cavity.

DDot and Large Cavity Probe response to Filament (shot 2 and 5)

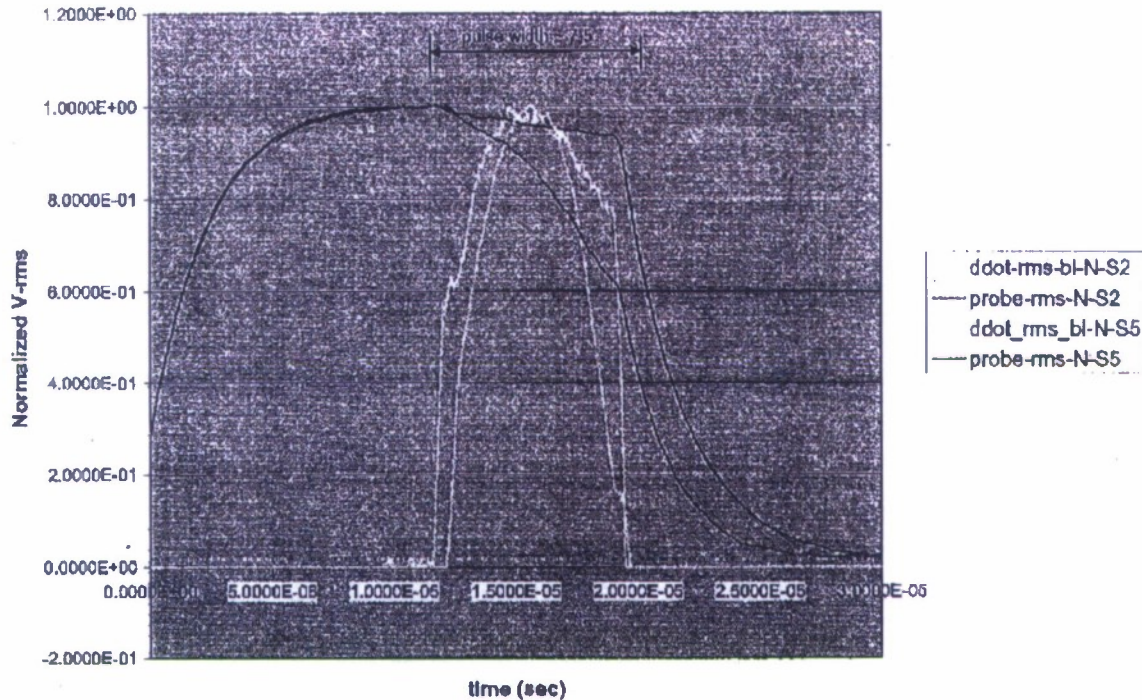


Figure 16
Cavity A, short focus attachment

Upon introduction of the laser pulse at $\sim 10 \mu\text{s}$ shown in figure 16, there is an obvious decrease in field inside the resonant chamber. This decrease in electric field corresponds to an increase in electric field outside the chamber as recorded by the D-dot. It is noteworthy that with this configuration, the pulse width of the RF energy observed outside of the chamber was $\sim 7.5 \mu\text{s}$, considerably longer than the $\sim 100 \text{ ns}$ lifetime of the filament or plasma alone. This lead to the belief that not only is the RF coupling onto the laser filament out of the cavity, but also that the RF is increasing the lifetime of the plasma filament by orders of magnitude. As anticipated, the high RF field strength is feeding and enhancing the plasma filament.

The expressions for the field inside a cylindrical resonant cavity from a typical microwave engineering or E&M reference to calculate the electric field present in this resonant chamber (ref. 23) can be used.

$$E_z = -\frac{j}{k} A \sqrt{\frac{\mu_0}{\epsilon_0}} J_0(kr) e^{j\omega t}$$

for the TM₀₁₀ mode in the cavity, where $k = 2.405/R_0$, and R_0 is the radius of the cavity. Using this equation for the electric field, the amplitude A can be determined as a function of measurable parameters using the previous equation for E_z and the unloaded Q of the cavity:

$$Q = 2\pi \text{ (energy stored/energy dissipated per cycle)}$$

where the energy dissipated per cycle is actually the power per cycle fed into the cavity. It then follows that the amplitude

$$A = \sqrt{\frac{2QPk^2}{\omega\mu\pi LR_0^2 J_1^2(kR_0)}}$$

where P is the input power, L is the cavity length, and ω the RF driving frequency. The amplitude A is related to the maximum electric field inside the cavity E_0 for the TM₀₁₀ mode via the relation

$$E_0 = \frac{A}{k} \sqrt{\frac{\mu_0}{\epsilon_0}}$$

Therefore, the maximum electric field inside our cylindrical resonant cavity for the TM₀₁₀ mode is

$$E_0 = \frac{1}{\pi} \sqrt{\frac{PQ}{\epsilon_0 f L R_0^2 J_1^2(kR_0)}}$$

For this cavity (cavity A), the parameters are shown in table 1.

Table 1
Cavity A, experimental parameters

Input power	$P = 830 \text{ W}$
Q	7150
Cavity length	$L = 98.2 \text{ mm}$
Cavity radius	$R_0 = 133.5 \text{ mm}$
RF frequency	$f = 897.77 \text{ MHz}$

Inputting the parameters from table 1 into the equation for E_0 , gives our predicted value for the maximum electric field $E_0 \sim 400 \text{ kV/m}$.

As mentioned earlier, without the necessary facilities at hand it was not possible to accurately calculate the effective area (and thus the gain) of the cavity probe sensor. Therefore, those measurements will be taken as a qualitative observation of the cavity field buildup and dump, rather than a quantitative one. The time scale, however, is still relevant and is helpful for making estimates of quantities such as cavity reactive power.

This experiment validated the theory of conduction of RF through a plasma filament with sufficient electron density. The experiment was repeated with a much longer focal length lens ($f = 1$ m), just enough to provide a much longer filament within the confines of the laboratory (fig. 17). In this case, it was observed that much shorter pulses coupled from the cavity, on the order of a few nanoseconds with a corresponding drop in cavity field amplitude as detected by the cavity probe. The decrease in amplitude of the cavity field was of a much smaller magnitude than for the case of the short focus plasma. This was expected due to the lower energy levels coupled out of the cavity in the form of the small pulses versus those with much longer pulse widths for the short focal length. Less energy was coupled out; therefore, the cavity field disturbance was also substantially smaller.

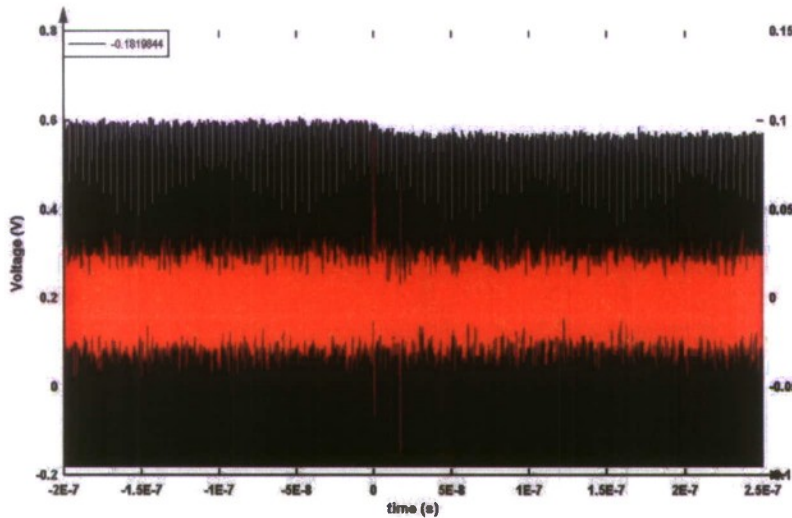


Figure 17
Cavity A, long focus attachment

GHz Resonant Cavity. The experiment from the previous section was repeated, this time using a much smaller cavity designed to operate at ~ 2.5 GHz [cavity B (fig. 18)]. The setup for this experiment was the same as the previous one with the exception of the high power RF source. For this test, the source was a traveling wave tube (TWT) RF source capable of delivering pulses above $10\ \mu\text{s}$ with $> 2\ \text{kW}$ of power. With this configuration a lower Q was achieved, $Q \sim 3080$, but the amplifier drive power was higher. Using the same relations as in the previous section, we calculated a maximum theoretical electric field inside the chamber, $E_0 \sim 841\ \text{kV/m}$ was calculated. This may be somewhat counterintuitive based upon the significantly lower Q for this chamber, however the higher input power and smaller dimensions play a large role in this calculation and the field in this case is actually twice that in cavity A. The relationship between the two cavities was predicted using the standard circular resonant cavity equations discussed in the previous section.

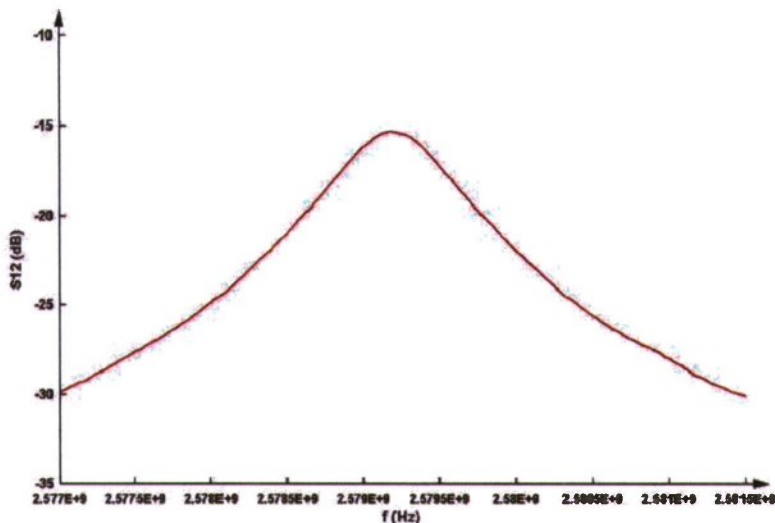


Figure 18
Q, cavity B

For this chamber, we again looked at both strong plasma created by a short focal length lens as well as a much longer filament (or small bundle of filaments) as in the case of Cavity A (table 2).

Table 2
Cavity B, experimental parameters

Input power	$P = 1300$ W (after cable loss)
Q	3080
Cavity length	$L = 35.5$ mm
Cavity radius	$R_0 = 51$ mm
RF frequency	$f = 2.579$ gHz

A build up time in the cavity was observed as expected and then a stable field inside the cavity with the absence of a laser pulse (fig. 19).

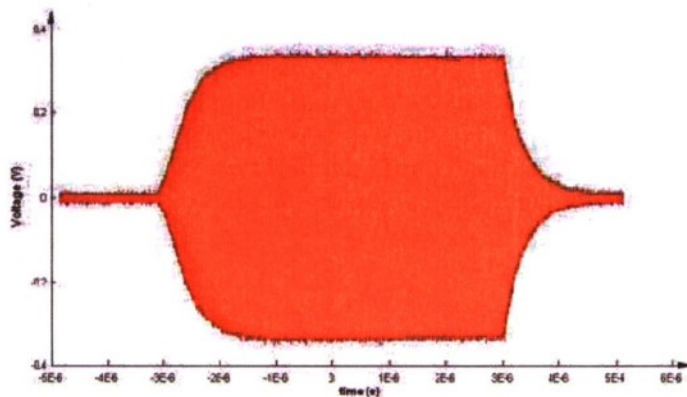


Figure 19
Cavity B, field resonance

Figure 20 shows the interaction for the case of the short focal length, short plasma filament interaction in the cavity. There is an initial, short pulse from the cavity to the outside along the channel and corresponding dip in the probe field followed by a second much longer and higher amplitude pulse.

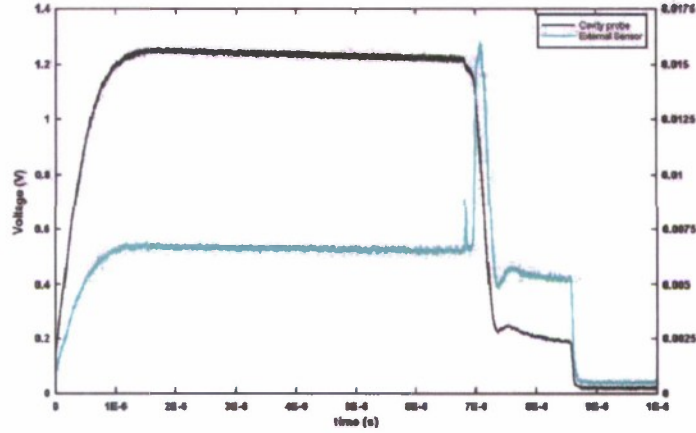


Figure 20
Cavity B, short focus attachment

The experiment was then repeated for cavity B with a longer, less intense plasma filament gently focused with a 1 m plano-convex lens. In this case (fig. 21), the interaction pulse width was much shorter (~10 ns) and only a portion of the cavity amplitude was attached to the filament and coupled from the resonant cavity.

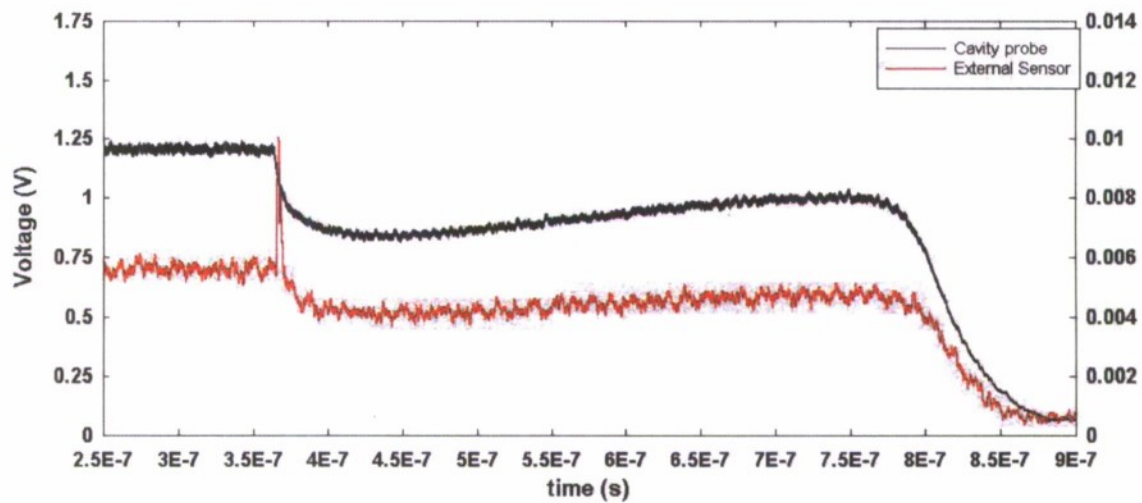


Figure 21
Cavity B, long focus attachment

This result was expected due to the reduced electron density in this case. Here, the plasma was formed mainly as a result of Kerr self-focusing, where in the case for the short focus the optical focus itself is more dominant.

As expected, both cavities reacted similarly when interacting with short and long filaments. Also the higher electric field in the small cavity translated to a greater portion of energy coupled from the cavity, validating the need to optimize electron density for ideal attachment and validating the trend for two different cavities and frequencies. It was also observed that chirp played a significant role in the extent of coupling to the filament. For each case, the chirp was adjusted via a micrometer controlled translation stage on the grating in the compressor at the output of the laser system. By tuning the chirp with the compressor, there was more control over where in space self-focusing would occur.

Planned Follow-up Test: Free Space Filament/Open-ended Rectangular Waveguide Attachment, TE Mode

This series of tests will represent the first trials of free space coupling of RF to the plasma filaments without a resonant cavity. The experimental setup will include a much higher power RF source at ~9 GHz capable of producing >500 kW. With this high power RF source, it was hoped that electric field levels comparable to those inside the resonant cavities are created in order to enhance electron density and assist with RF coupling to the filament(s). An attempt to couple to the TE mode of a waveguide section as was done for the case of the copper wire in the beginning of this section will be made. Other modes of coupling to the filament will also be investigated in order to achieve the best impedance match.

Laser energy upgrades are planned that will allow for propagation of higher energy pulses in pairs, allowing the investigation of TEM mode coupling in free space in addition to single plasma wire coupling.

THEORY AND MODELING

Basic Theory

For the purposes of this research, the laser generated filament can be considered as a cylindrical wire in space. The EM theory can then be used to predict how various modes of RF will propagate down the wire or pair of wires and the resulting attenuation of the RF energy as a function of distance.

Let's begin with the foundations for this model and further develop the details and assumptions. Recall, the laser generated filament is in effect a plasma, or an ionized gas with relatively equal ion and electron densities.

Beginning with the relation for the electric displacement

$$\mathbf{D} = \epsilon_0 \mathbf{E} + \mathbf{P} \text{ (C/m}^2\text{)}$$

where ϵ_0 is the permittivity of free space $8.854 \times 10^{-12} \text{ m}^{-3} \text{ kg}^{-1} \text{ s}^4 \text{ A}^2$, \mathbf{E} represents the electric field and \mathbf{P} the polarization vector. The polarization vector can also be represented as $\mathbf{P} = N \mathbf{p}$, where N is the electron density or number of electrons per unit volume and \mathbf{p} represents the electric dipole moment. The force on an electron of charge $-e$ in an electric field \mathbf{E} can be defined using $\mathbf{F} = m\mathbf{a}$, or

$$-e\mathbf{E} = m \frac{d^2}{dt^2} \mathbf{x} = -m\omega^2 \mathbf{x}$$

Defining the dipole moment $\mathbf{p} = -e \mathbf{x}$, where e is the electron charge and \mathbf{x} is distance and using the previous equations a new definition for the displacement \mathbf{D} is achieved.

$$\mathbf{D} = \epsilon_0 \left(1 - \frac{\omega_p^2}{\omega_2} \right) \mathbf{E}$$

where ω_p represents the plasma angular frequency (ref. 21)

$$\omega_p = \sqrt{\frac{e^2 N}{m \epsilon_0}} \text{ (rad/s)}$$

As discussed at the beginning of this report, the electron density of our plasma filaments was determined to be on the order of $n_e \sim 10^{16} \text{ cm}^{-3}$. However, this may vary depending on the conditions of the atmosphere, characteristics of the laser pulse and other means used to create the filament. The theoretical examination the dependence of attenuation in the plasma wire with respect to changes in electron density will be examined. In general, the value as calculated optically as $N \sim 10^{16} \text{ m}^{-3}$ resulting in a plasma angular frequency $\omega_p \sim 5.6 \times 10^9 \text{ rad/s}$ and the plasma frequency $f_p = \omega_p/2\pi \sim 0.9 \text{ GHz}$ will be used.

Single Wire Filament

Let's now define the electric and magnetic field components of the plasma wire in cylindrical coordinates for the case of a single wire as shown in figure 22.

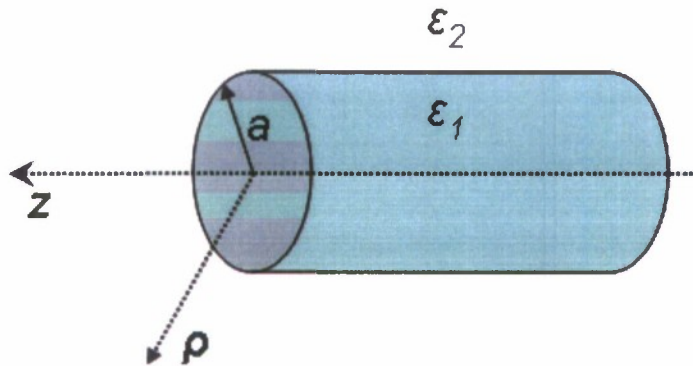


Figure 22
Wire, cylindrical coordinates

In figure 22, ϵ_1 and ϵ_2 represent the permittivity inside and outside of the wire cylinder, respectively. The complex permittivity inside the wire ($p < a$) as a function of ω is defined as

$$\epsilon_1(\omega) = 1 - \left(\frac{\omega_p^2}{\omega(\omega + i\nu)} \right)$$

where ν represents the electron scattering frequency, which is assumed to be $\sim 10^{13}$.

The derivation of the components of the electric and magnetic field inside the plasma wire can begin by assuming a wave propagating down the z-axis or long direction of the wire and thus having a time harmonic dependence of $e^{i(hz-\omega t)}$. [This derivation follows those found in Jackson (ref. 24) or Pozar (ref. 17) and many other E&M textbooks]. Begin with Maxwell's equations in their general form

$$\nabla \cdot \vec{E} = \frac{\rho}{\epsilon_0}$$

$$\nabla \times \vec{B} - \frac{\partial \vec{E}}{c^2 \partial t} \mu_0 J \quad \text{where } \vec{D} = \epsilon_0 \vec{E} \text{ and } \vec{B} = \mu_0 \vec{H}$$

$$\nabla \times \vec{E} + \frac{\partial \vec{B}}{\partial t} = 0$$

$$\nabla \cdot \vec{B} = 0$$

Incorporate the time harmonic dependence and rewrite the electric and magnetic fields in cylindrical coordinates as

$$\vec{E}(\rho, \phi, z) = [\bar{e}(\rho, \phi) + \hat{z}e_z(\rho, \phi)]e^{i(hz-\omega t)}$$

$$\vec{H}(\rho, \phi, z) = [\bar{h}(\rho, \phi) + \hat{z}h_z(\rho, \phi)]e^{i(hz-\omega t)}$$

Using these field equations, rewrite two of Maxwell's equations for the case of the plasma wire as

$$\nabla \times \vec{E} = i\omega \mu \vec{H}$$

$$\nabla \times \vec{H} = i\sigma \epsilon \vec{E}$$

From these equations, the components of the E and H fields can be determined as follows

$$i\omega \mu H_\phi = ihE_\rho - \frac{\partial E_z}{\partial \rho}$$

or

$$H_\phi = \frac{h}{\omega \mu} E_\rho - \frac{1}{i\omega \mu} \frac{\partial E_z}{\partial \rho}$$

Similarly,

$$-i\omega \epsilon E_\phi = \frac{\partial H_z}{\partial \phi} - ihH_\phi$$

or

$$E_\phi = \frac{-1}{i\omega \epsilon} \frac{\partial H_z}{\partial \phi} + \frac{h}{\omega \epsilon} H_\phi$$

Then plug the previous equation for H_ϕ into the equation for E_ϕ resulting in a simplified expression for E_ϕ . Similarly, we can arrive at the expressions for E_ρ , H_ϕ , and H_ρ following similar theoretical work done on dielectric rod approximations for fiber (ref. 25).

$$E_\rho = \frac{ih}{k_\perp^2} \left(\frac{\partial E_z}{\partial \rho} + \frac{\omega \mu}{h} \frac{1}{\rho} \frac{\partial H_z}{\partial \phi} \right) \quad H_\rho = \frac{ih}{k_\perp^2} \left(\frac{\partial H_z}{\partial \rho} - \frac{\omega \varepsilon}{h} \frac{1}{\rho} \frac{\partial E_z}{\partial \phi} \right)$$

$$E_\phi = \frac{ih}{k_\perp^2} \left(\frac{1}{\rho} \frac{\partial E_z}{\partial \phi} - \frac{\omega \mu}{h} \frac{\partial H_z}{\partial \rho} \right) \quad H_\phi = \frac{ih}{k_\perp^2} \left(\frac{1}{\rho} \frac{\partial H_z}{\partial \phi} + \frac{\omega \varepsilon}{h} \frac{\partial E_z}{\partial \rho} \right)$$

where $k_\perp^2 = \omega^2 \varepsilon \mu - h^2$

The z-components for the E and H fields must then be determined. Begin with the Helmholtz equations for the charge-free dielectric region inside of the plasma wire in order to get the electric and magnetic field intensities.

$$\nabla^2 \vec{E} + k^2 \vec{E} = 0 \quad \text{where } k = \omega \sqrt{\mu \varepsilon}$$

$$\nabla^2 \vec{H} + k^2 \vec{H} = 0$$

∇^2 , the Laplacian operator, can be separated into two parts for convenience due to the geometry of the cylinder that is being considered. Specifically, one part for the transverse coordinates $\nabla_{\rho\phi}^2$ and another for the axial or z-component ∇_z^2 . Then rewrite the electric and magnetic fields as a sum of these two components

$$\vec{E} = E_T + a_z E_z$$

$$\vec{H} = H_T + a_z H_z$$

As mentioned earlier the TE mode in this single wire scenario will be examined. For the case of the TE mode, boundary conditions, which require $E_z = 0$ and $H_z \neq 0$, can be defined. This follows from the definition of a TE wave that states that the electric field components lie solely in the transverse direction. The field components of the H-field will be expressed in terms of $H_z = H_{z0} e^{-\gamma z}$ and write another Helmholtz equation

$$\nabla_T^2 H_z + (k^2 + \gamma^2) H_{z0} = 0$$

or

$$\nabla_T^2 H_z + h^2 = 0, \text{ where } h^2 = (k^2 + \gamma^2)$$

The Helmholtz equation can then be expanded into cylindrical coordinates

$$\frac{1}{\rho} \frac{\partial}{\partial \rho} \left(\rho \frac{\partial H_z}{\partial \rho} \right) + \frac{1}{\rho^2} \frac{\partial^2 H_z}{\partial \phi^2} + h^2 z = 0 \quad (1)$$

This Helmholtz, second order differential equation can be solved using separation of variables.

$$H_z(\rho, \phi) = P(\rho) \Phi(\phi) \quad (2)$$

Then substituting equation 2 into equation 1 and dividing by the product $P(\rho)\Phi(\phi)$ yields the separated relation:

$$\frac{\rho}{R} \frac{d}{d\rho} \left(\rho \frac{dR(\rho)}{d\rho} \right) + h^2 r^2 = \frac{-1}{\Phi} \frac{d^2 \Phi}{d\phi^2} \quad (3)$$

For equation 3 to be valid, both sides of the equation must be equal to a constant, called n^2 . Using this constant, equation 3 can be broken into two separate ordinary differential equations

$$\frac{d^2 \Phi(\phi)}{d\phi^2} + n^2 \Phi(\phi) = 0 \quad (4)$$

and

$$\frac{\rho}{P(\rho)} \frac{d}{d\rho} \left[\rho \frac{dP(\rho)}{d\rho} \right] + h^2 r^2 = n^2 \quad (5)$$

The second equation can be rearranged to take on the form of a Bessel differential equation

$$\frac{d^2 P(\rho)}{d\rho^2} + \frac{1}{r} \frac{dP(\rho)}{d\rho} + \left(h^2 - \frac{n^2}{r^2} \right) P(\rho) = 0$$

Solutions to a Bessel equation of this type can be determined by assuming a power series in ρ with unknown coefficients

$$P(\rho) = \sum_{p=0}^{\infty} C_p (k_{11}\rho)^p$$

The result of this power series can be expressed as

$$P(\rho) = C_n J_n(k_{11}\rho), \text{ where } C_n \text{ is a constant}$$

Here J_n represents a Bessel function of the first kind given by the expression

$$J_n(h\rho) = \sum_{m=0}^{\infty} \frac{(-1)^m (k_{11}\rho)^{n+2m}}{m! (n+m)! 2^{n+2m}}$$

This expression holds for integral values of n ; however, the Bessel equation is a second order equation, therefore, there should be two linearly independent solutions. The second solution is known as a Neumann function or a Bessel function of the second kind and is given by the expression

$$N_n(h\rho) = \frac{\cos(n\pi) J_n(k_{11}\rho) - J_{-n}(k_{11}\rho)}{(\sin n\pi)}$$

A general solution can now be written in terms of both the Bessel function of the first and second kind as

$$N_n(h\rho) = C_n J_n(k_{\perp 1}\rho) + D_n N_n(k_{\perp 1}\rho)$$

This solution can be further simplified by taking a closer look at the Bessel function characteristics. This Neumann function has a unique property that it becomes zero for values of $n = 0$. For the case of the symmetrical, cylindrical wire, the case $\rho = 0$ must be examined, which represents the center axis (fig. 22). Therefore, the $D_n N_n(h\rho)$ term from our equation can be thrown out and left with two equations for both the region inside the wire and the region outside of the wire, representing the z component of the E and H fields. Taken into account was that all components of the solution are periodic with ϕ so the only solutions to equation 4 are sine and cosine or some linear combination of sine and cosine giving the following four equations, where similar actions have also been taken to arrive at the components outside of the wire.

$$E_z = A \cdot J_m(k_{\perp 1}\rho) \cdot \sin(m\phi + \phi_0) \quad \text{for } 0 \leq \rho \leq a$$

$$H_z = B \cdot J_m(k_{\perp 1}) \cdot \cos(m\phi + \phi_0) \quad \text{for } 0 \leq \rho \leq a$$

$$E_z = C \cdot K_m(\gamma_2\rho) \cdot \sin(m\phi + \phi_0) \quad \text{for } \rho \geq a$$

$$H_z = D \cdot K_m(\gamma_2\rho) \cdot \cos(m\phi + \phi_0) \quad \text{for } \rho \geq a$$

where $k_{\perp 1} = \sqrt{k_0^2 \varepsilon_1 \mu_1 - h^2}$ and $\gamma_2 = \sqrt{h^2 - k_0^2 \varepsilon_2 \mu_2}$

Applying the boundary conditions, specifically that the normal component of H is continuous and the tangential E is continuous, we can arrive after some rather tedious algebra and substitution of the permittivity calculated earlier in this section, at the general dispersion equation for the E_m and H_n modes of the wire.

$$\left(\frac{\varepsilon_1}{\varepsilon_2} f - F\right) \left(\frac{\mu_1}{\mu_2} f - F\right) = \frac{m^2 (ha)^2 (k_0 a)^2}{(\gamma_2 a)^4 (k_{\perp 1})^4} (\varepsilon_1 \mu_1 - \varepsilon_2 \mu_2)^2 \quad (6)$$

where

$$f = \frac{m}{(k_{\perp 1} a)^2} - \frac{J_{m+1}(k_{\perp 1} a)}{J_m(k_{\perp 1} a)} \cdot \frac{1}{(k_{\perp 1} a)}$$

$$F = \frac{m}{(\gamma_2 a)^2} - \frac{K_{m-1}(\gamma_2 a)}{K_m(\gamma_2 a)} \cdot \frac{1}{\gamma_2 a}$$

Next, examine the interface between the region inside the wire and the region outside of the wire. The interface between the air and the plasma wire can be represented by figure 23 using this approximation.

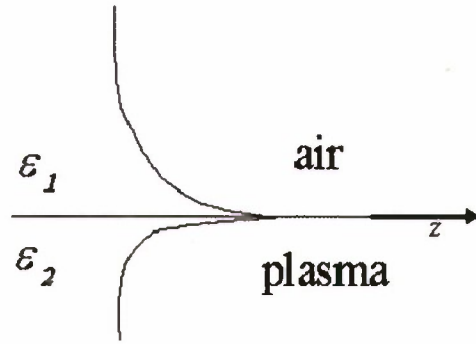


Figure 23
Air/plasma interface

k_z is defined and the resulting formula for the attenuation along the plasma wire D as

$$k_z = k_0 \sqrt{\frac{\epsilon_1(\omega) \cdot \epsilon_2}{\epsilon_1(\omega) + \epsilon_2}}$$

$$D = \frac{20}{1n(10)} \operatorname{Im} k_z$$

$$[D] = \frac{dB}{m}, [k_z] = \frac{1}{m}$$

Move on to find the exact solution by setting equation 6 equal to zero and solving for the complex root(s). As an example for a plasma wire of diameter $d = 1$ cm, an RF frequency $f \sim 3$ GHz, calculate a complex permittivity $\epsilon = 0.709 + 154.3i$, corresponding to $D \sim 15.3$ dB/m. Figure 24 plots the dispersion versus the complex and real values of h multiplied times the wavelength λ_0 .

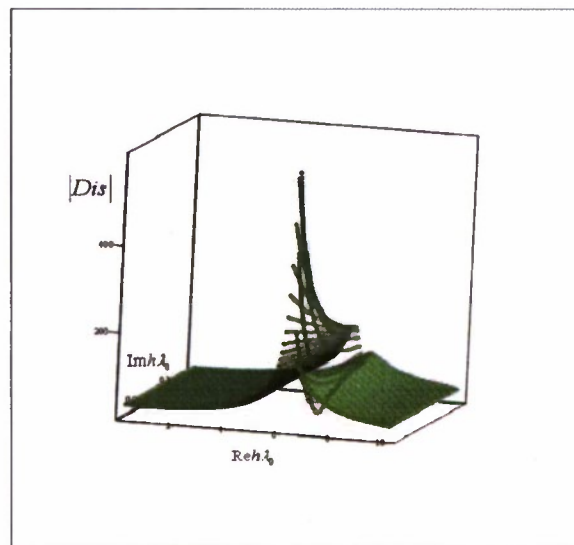


Figure 24
Dispersion versus $\operatorname{Re}h\lambda_0, \operatorname{Im}h\lambda_0$

With the previous equations, the attenuation along the length of the wire as a function of frequency can be plotted. The attenuation coefficient D will also depend on the electron density n . Therefore, plot D will also be plotted for various values of n to show the attenuation trend as a function of electron density of the filament. Assuming an electron density on the order of 10^{16} cm^{-3} , as indicated in the literature, the attenuation of an RF pulse attached to a plasma filament versus one propagating in free space can be plotted (fig. 25). It is evident from figure 25 that for a completely attached EM wave (3 GHz, $d \sim 0.01$ m), a loss of greater than 2 dB/m will severely limit the propagation range.

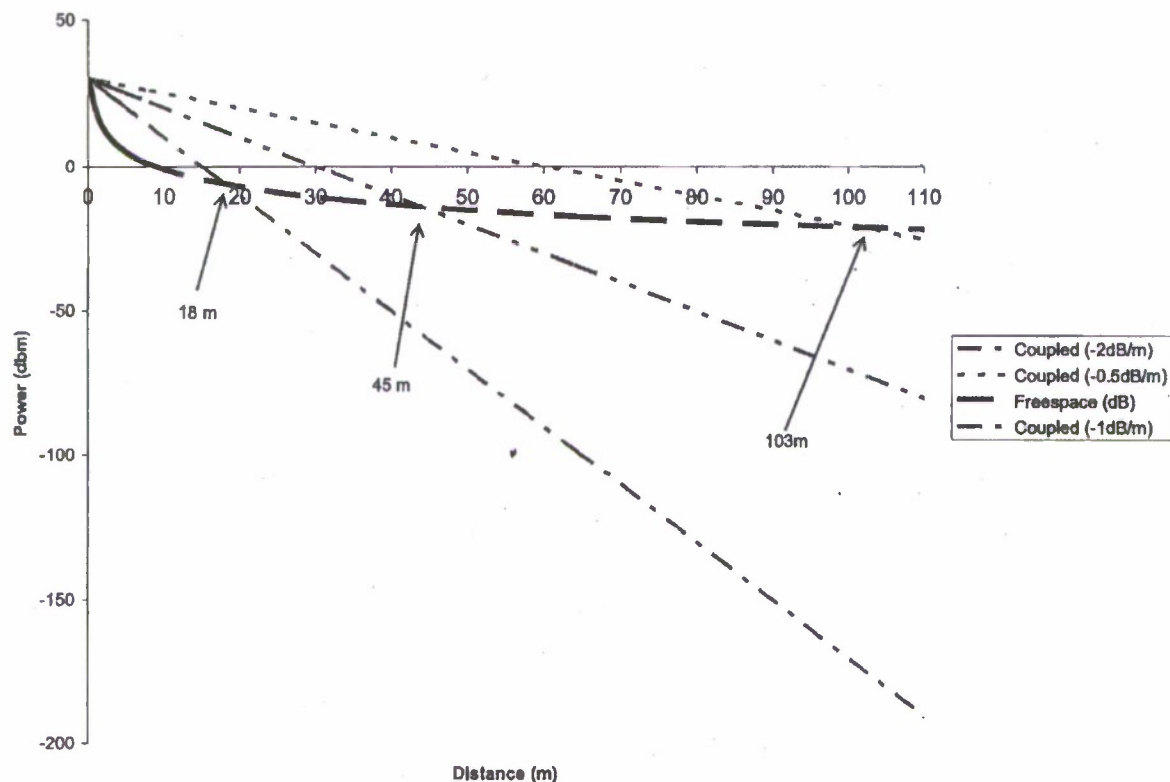


Figure 25
Coupled versus free-space propagation

Two Plasma Wires

Let's now examine the case where there are two plasma wires separated by some distance d as shown in figure 26.

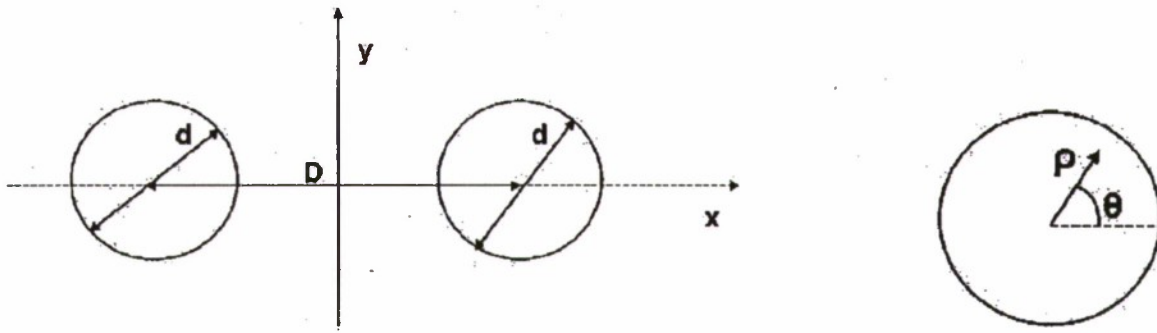


Figure 26
Dual wire geometry

For this scenario, transmission of the TEM mode traveling on a two wire transmission line consisting of two plasma channels will be looked at. A perturbation method for calculating attenuation along a lossy transmission line similar to the approach used by Pozar in his microwave engineering text (ref. 17) will be used. Begin with the power equation for a TEM transmission line

$$P = P_0 e^{-\alpha z}$$

P corresponds to the power of the RF signal propagating along the wire pair and α , the attenuation or loss encountered during transmission. For this case, the attenuation α , is proportional to the electric field inside the plasma wires and is given by

$$\alpha = \omega \text{Im}(\epsilon_{\text{wire}}) \frac{\iint |\vec{E}(\rho, \theta)|^2}{P_0} \frac{\text{wire cross-section}}{\rho d \rho d\theta}$$

ω is the frequency of RF multiplied by a factor of 2π and the imaginary part of ϵ_{wire} is given by

$$\text{Im}(\epsilon_{\text{wire}}) = \epsilon_0 \frac{\omega_p^2 \nu}{\omega(\omega^2 + \nu^2)}$$

where ω_p^2 is the plasma frequency as defined in the previous section and ν is the electron scattering frequency. Finally, the electric field, $\vec{E}(\rho, \theta)$ inside the wire is calculated using perturbation theory.

Let's begin with the electric and magnetic field equations in terms of the vector potential \vec{A} .

$$\vec{H} = \frac{1}{\mu} \vec{\nabla} \times \vec{A}$$

and

$$\vec{E} = -\vec{\nabla} \Phi - \frac{\partial \vec{A}}{\partial t}$$

As in the case of the single plasma wire, we are again considering a traveling wave with harmonic time dependence of the form $e^{i(hz-\omega t)}$. Also, symmetry along the z-axis of the wire allows us to define $\vec{A} = \varphi_A \cdot \vec{z}_0$. Therefore, taking into account the harmonic dependence of our EM wave, we can rewrite the equation for the electric field \vec{E} as

$$\vec{E} = i\omega\varphi_A \cdot \vec{z}_0 - \vec{\nabla}_\perp \varphi - \vec{\nabla}_z \varphi$$

where the divergence of the potential ϕ has been broken down into two parts, one along the length of the wire or the z-component and the other the perpendicular components normal to the z-component. Again, as in the single wire case the symmetry of the wire along the z-axis allows us to further reduce the equation for the electric field above to

$$\vec{E} = \vec{z}_0(i\omega\varphi_A - ih\varphi) - \vec{\nabla}_\perp \varphi$$

In free space, $i\omega\varphi_A$ is equal to $ih\varphi$, thus eliminating the \vec{z}_0 term resulting in $\vec{E} = -\vec{\nabla}_\perp \varphi$ also taking note that $\vec{\nabla}_\perp \cdot (\vec{\nabla}_\perp \varphi) = 0$. In the wire, on the other hand, $\vec{\nabla}_\perp \varphi \cong 0$ so the z-component of the electric field becomes

$$E_z = \vec{z}_0(i\omega\varphi_A - ih\varphi)$$

The magnetic field equation inside the wire can be rewritten as

$$\vec{H} = \frac{1}{\mu_p} \vec{\nabla} \times (\varphi_A \cdot \vec{z}_0) = \frac{1}{\mu_p} (\vec{\nabla}_\perp \varphi_A) \times \vec{z}_0$$

Taking the curl of \vec{H}

$$\vec{\nabla} \times \vec{H} = \vec{J} + \frac{\partial \vec{D}}{\partial t} \cong \sigma * E_z \cdot \vec{z}_0$$

By setting the two equations for the curl of the magnetic field equal to one another, the following relation is

$$\vec{\nabla} \times \vec{H} = -\vec{z}_0 \cdot \left(\vec{\nabla}_\perp \cdot \left(\frac{1}{\mu_p} \vec{\nabla}_\perp \varphi_A \right) \right) = \sigma * E_z \cdot \vec{z}_0 = \sigma(i\omega\varphi_A - ih\varphi)\vec{z}_0$$

Two relations follow: the first for inside the metal and the second in air, respectively

$$(\vec{\nabla}_\perp^2 + i\omega\sigma\mu_p)\varphi_A = ih\sigma\mu_p \quad (5)$$

$$(\vec{\nabla}_\perp^2)\varphi_A = 0 \quad (6)$$

The electric and magnetic field equations for both are written in the metal and in the air region

$$\vec{H} = \frac{\vec{\nabla}_\perp \varphi_A \times \vec{z}_0}{\mu_p} \quad (\text{metal}) \quad (9)$$

$$\vec{E} = -\vec{z}_0 \cdot \frac{\vec{\nabla}_\perp^2 \varphi_A}{\mu_p \sigma} \quad (\text{metal})$$

$$\vec{H} = \vec{H}_0 = \frac{\vec{\nabla}_\perp \varphi_{A,0} \times \vec{z}_0}{\mu_p} \quad (\text{air}) \quad (10)$$

$$\vec{E} = \vec{E}_0 = -\vec{z}_0 \cdot \frac{\vec{\nabla}_\perp \varphi_{A,0}}{\sqrt{\mu_0 \epsilon_0}} \quad (\text{air})$$

$\varphi_{A,0}$ for a two wire transmission line can be defined as

$$\varphi_{A,0} = \mu_0 I_0 1n \left(\frac{\left(x - \frac{D}{2} - b \right)^2 + y^2}{\left(x - \frac{D}{2} + b \right)^2 + y^2} \right)^{1/2}, \text{ where } b = \sqrt{\left(\frac{D}{2} \right)^2 - \left(\frac{d}{2} \right)^2} \quad (11)$$

I_0 represents the total current along the wire, μ_0 is free space permittivity constant which in this case is also equal to μ_p , the magnetic permittivity of plasma in equation 9. Taking into account the continuity of the boundary conditions of the tangential components of \vec{E} and \vec{H} between the surface of the wires and the air yield the following two equations for the surface of the wires

$$\vec{n} \cdot \left(\frac{1}{\mu_p} \vec{\nabla}_\perp \varphi_A - \frac{1}{\mu_0} \vec{\nabla}_\perp \varphi_{A,0} \right) = 0$$

$$\varphi_{A,0} = \varphi_A$$

Employing the equations at the boundary conditions, a solution in terms of Bessel functions, which is intuitive due to the cylindrical nature of the plasma wires can be looked for. Looking at one wire, which is possible due to symmetry, can write the field in on wire in terms of

$$\varphi_A = \sum_{m=0}^{\infty} \varphi_m J_m(k\rho) \cdot \cos(m\theta)$$

With boundary conditions

$$\frac{1}{\mu_p} \frac{\partial \varphi_A}{\partial \rho} \left(\rho = \frac{d}{2}, \theta \right) \equiv \frac{1}{\mu_0} \frac{\partial \varphi_{A,0}}{\partial \rho} \left(\rho = \frac{d}{2}, \theta \right)$$

Then applying these boundary conditions to equation 11 and integrate over the angle θ , the result is the following Bessel harmonics amplitudes

$$\varphi_m = \frac{-I_0 \mu_0}{\pi * k \frac{d}{2} \delta_m J'_m \left(k \frac{d}{2} \right)} \left(\frac{D}{d} - \sqrt{\left(\frac{D}{d} \right)^2 - 1} \right)^2 - 1, \text{ where } \delta_m = 1, \text{ if } m > 0, \delta_m = 2, \text{ if } m = 0$$

with $k^2 = i\omega\sigma\mu_0$ and $\sigma = \epsilon_0 \frac{\omega_p^2 v}{(\omega^2 + v^2)}$ the plasma conductivity.

Now, there is an expression for the exact electric field inside the wire

$$\vec{E} = -\vec{z}_0 \cdot \frac{\vec{\nabla}_\perp^2 \varphi_A}{\mu_p \sigma} = -\vec{z}_0 \frac{-i\omega\sigma\mu_p \varphi_A}{\mu_p} = \vec{z}_0 i\omega \varphi_A$$

Along with this equation for the electric field for the wire the current I_0 can be replaced with the propagating power P_0 by taking into account the impedance of the TEM mode, which can be looked up in many references (ref. 21)

$$P_0 = \frac{1}{2} Z_{TEM} \cdot |I_0|^2$$

where Z_{TEM} is given as

$$Z_{TEM} = \sqrt{\frac{\mu_0}{\epsilon_0}} \frac{1}{\pi} \ln \left(\frac{D}{d} + \sqrt{\left(\frac{D}{d} \right)^2 - 1} \right)$$

Finally, taking into account the exact electric field in the wires and the propagating power P_0 , the expression for the total absorption losses of the TEM mode traveling through a pair two non-ideal wires can be rewritten as

$$\alpha = \frac{32 \cdot \omega \cdot \mu_0}{(2\pi)^2 Z_{TEM} \cdot d^2} \cdot \left[\iint_{\substack{0 < \rho < d/2 \\ 0 < \theta < 2\pi}} \left| \sum_{m=0}^{\infty} \frac{\left(\frac{D}{d} - \sqrt{\left(\frac{D}{d} \right)^2 - 1} \right)^m}{\delta_m \cdot J'_m \left(k \frac{d}{2} \right)} \cdot J_m(k\rho) \cdot \cos(m\theta) \right|^2 \rho d\rho d\theta \right]$$

Using this equation, the consequences of the propagation constant α as a function of our system conditions can be investigated further.

Let's begin by examining the effect of electron density and its impact on attenuation for the case of the two wire system. Figure 27 shows the decrease in attenuation and subsequently, the increased in coupling efficiency with increasing electron density.

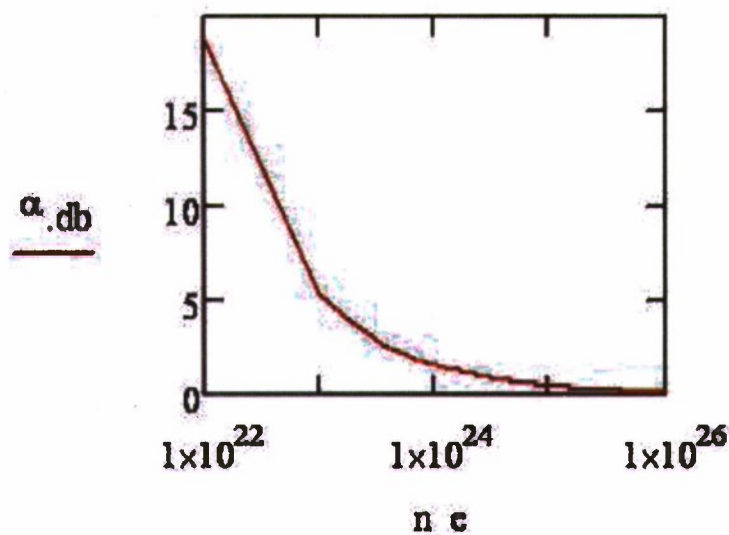


Figure 27
Dual wire attenuation as a function of electron density

As described earlier, this increased coupling efficiency with higher electron density is a direct consequence of the increased conductivity of the plasma channels. As the electron density increases, the plasma channels behave more and more like copper conductors and less like lossy dielectrics. This also demonstrates that it is necessary to optimize and if possible, enhance the electron density of the plasma channels as much as possible to achieve any substantial attachment of the EM waves regardless of the number of plasma conductors.

Next, the relationship between attenuation and frequency for the two plasma wire scenario will be investigated. As in the case of the single plasma wire; the general trend is that the higher the frequency, the higher the attenuation (fig. 28).

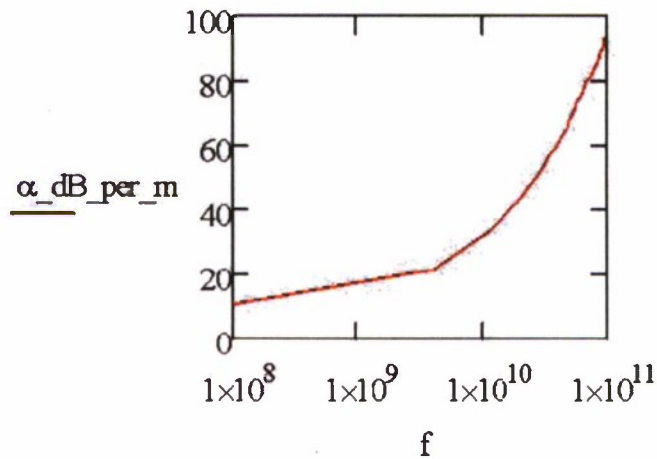


Figure 28
Dual wire attenuation as a function of frequency

The role the diameter of the plasma wire has in determining attenuation in the two wire system will also be looked at. Again, as in the case for the single wire, attenuation is reduced for larger diameters of plasma (fig. 29).

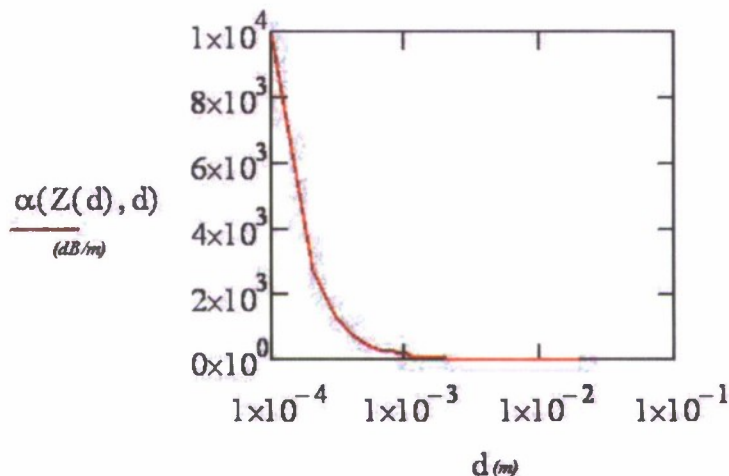


Figure 29
Dual wire attenuation as a function of wire diameter

As one would expect, these parameters are innate to coupling along a plasma wire in general and should not change drastically from the case of single wire to dual wire systems. However, when the focus is on the orientation of the two plasma wires, some significant trends can be seen. Figure 30 shows the attenuation for a two plasma wire system as a function of the wire separation, characterized in terms of the RF wavelength λ . These somewhat unexpected results show that the propagation loss actually decreases as the separation increases up to a value of 2λ . It should be noted however, that this model assumes that the source and antenna system is able to supply constant power to both wires regardless of separation. Therefore, these results must be used with consideration of source antenna characteristics. For the case of the two copper wires and small horn antenna, these results were consistent experimentally up to a value of 2λ . Most likely at separations much larger than this, coupling will fall off rapidly.

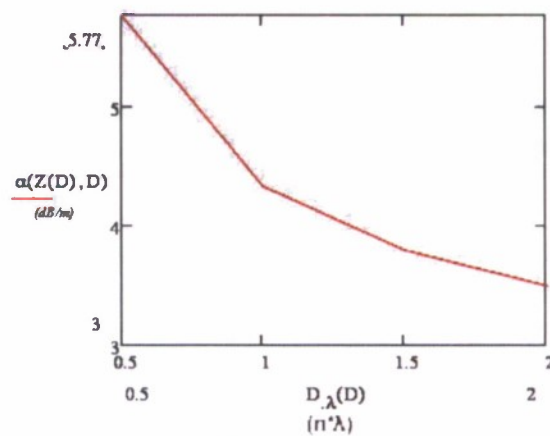


Figure 30
Dual wire attenuation as a function of wire separation

Based upon the results of the dual wire modeling effort, one could study parameters that are feasible in the laboratory and provide optimal results. Figure 31 illustrates an example of an RF source operating at 500 MHz, with spacing equal to twice the wavelength and various reasonable filament bundle diameters. Attenuation is shown for each of these plasma bundle diameters as a function of electron density [the expected electron density of 10^{22} (m^{-3}) and enhanced electron densities].

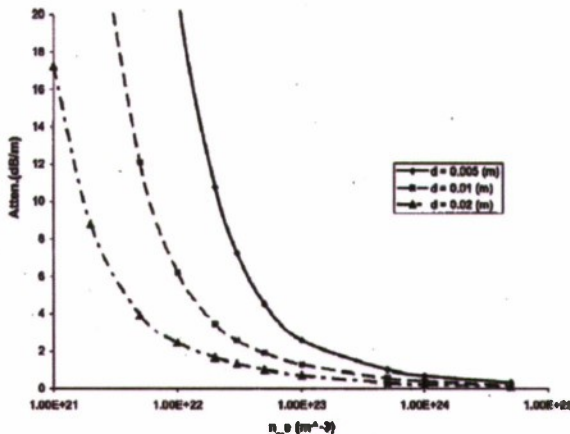


Figure 31
Attenuation as a function of electron density for feasible ideal cases

Figure 31 demonstrates a number of systems that could be designed for which the predicted attenuation would be well under 2 dB/m with some enhancement and ~2 dB/m without enhancement.

CONCLUSIONS AND SUMMARY

As demonstrated, ultrafast laser generated plasma filaments offer the potential of a conductive channel that can be directed at will through the atmosphere over limited distances. The ability to harness and employ this potential would provide a means of delivering large amounts of radio frequency (RF) with less loss over longer distances. In the future, plasma filaments could potentially create directional transmission lines in air, which could be created, directed and destroyed nearly instantaneously.

This report examines the potential to harness the conductive properties of these filaments for RF attachment. Modeling and simulation show, under ideal conditions, the possible modes of coupling and losses as a function of source parameters. Experimental data demonstrates, albeit to a limited extent, filaments are in fact conductive. The possibility, however, to enhance this conductivity with the RF source itself appears promising.

It was shown that plasma filaments do in fact behave like lossy conductors and their behavior can be characterized by models treating them as such. Over longer distances, factors such as energy levels and plasma recombination rates and lifetimes, will be limiting factors.

Based upon the results of the theoretical work, the most efficient method for RF transmission after attachment to a plasma filament would be for the case of a two plasma wire transmission (TEM) mode, with a spacing of $\sim 2\lambda$ at a frequency in the megahertz (or more practically hundreds of megahertz) and with the highest electron density possible. Methods of

electron density enhancement are currently being explored and may in fact make this task significantly easier in the future.

Based upon theoretical modeling and experimental results, it was demonstrated that RF attachment to plasma filaments is in fact possible. Optimization of this phenomenon (after the initial coupling) requires filaments that look as much as possible to our RF source as an ideal wire. Follow up research will focus on electron density enhancement and high power free space transmission.

REFERENCES

1. Rae, S.C. Rae; Opt. Comm. 97, 25; 1993.
2. Rankin, R.; Capjack; C.E.; Burnett, N.H.; and Corkum, P.; Opt. Lett. 16, 835, 1991.
3. Hitoshi, H.; Kazuhiro, A.; et al.; ...*Rapid Communications* 3, 177; 2004.
4. Braun, A.; Korn, G.; Liu, X.; et al.; Optics Letts. 20, No. 1; 1995.
5. Gaeta, Alexander L.; Phys. Rev. Lett. 84, Number 16, 3582; 2000.
6. Diels, Jean-Claude; Ultrashort Laser Pulse Phenomena: Fundamentals, Techniques and Applications on a Femtosecond Time Scale, Academic Press.
7. Shen, Y.R. Shen; The Principles of Nonlinear Optics; Wiley-Interscience, New York, 1, pp. 303-324; 1984.
8. Gibbon, Paul; Short Pulse Laser Interactions with Matter, Imperial College Press.
9. Steinert, Roger; Ophthalmology Times Europe, Jan/Feb 2007.
10. National Science Foundation; "Laser "Scalpel" Improves Popular Eye Surgery; Ultrafast Pulse Offers High Precision for Cutting Corneal Flap;" *Science Daily*, 2001.
11. Rodriguez, M. and Sauerbrey, R., et. al.; Optics Lett., 27, No. 9, 772; 2002.
12. Hecht, Jeff (editor); Laser Focus World, September 2007.
13. Rulliere, Claude, Editor; *Femtosecond Laser Pulses: Principles and Experiments*, Advanced Texts in Physics.
14. <http://www.spectrogon.com/gratpulse.html#gratpcinfo>
15. Kasparian, J.; Sauerbrey, R.; Chin, S.L.; et al.; Appl. Phys. B 71, 877; 2000.
16. Ladouceur, H.D.; Baronavski, A.P.; Lohrmann, D.; Grounds, P.W.; Giradi, P.G.; Optics Comms. 189, 107-111; 2001.
17. Pozar, David M.; *Microwave Engineering*, Second Edition, Wiley.
18. Lewellen, J.W.; Noonan, J.; Phys. Rev. Special Topics - Accelerators and Beams, 8, 033502; 2005.
19. Aschroft, N.W. and Merimin, N.D; Solid State Physics, Saunders; 1976.
20. Goubau, G.; IRE Transactions on Microwave Theory and Techniques, 197; 1956.
21. Cheng, David K.; Field and Wave Electromagnetics, 2nd edition, Addison-Wesley.
22. Gurevich, A.V.; Borisov, N.D.; Milikh, G.M.; Physics of Microwave Discharges, Gordon and Breach Science Publishers.

23. Maier, Leonard C., Jr.; "Field Strength Measurements in Resonant Cavities;" Technical Report No. 143; Research Laboratory of Electronics; M.I.T.; November 2, 1949.
24. Jackson, Classic Electrodynamics, Third Edition, Wiley.
25. Raspoin, Alexander and Cui, Hong-Liang; "Calculation of Evanescent Field Interaction with Metallic Nanoparticles Immobilized on the Air Holes of Solid-Core Photonic Crystal Fiber;" Optics East; 2005.

DISTRIBUTION LIST

U.S. Army ARDEC
ATTN: RDAR-EIK
RDAR-GC
RDAR-WSW-A (4)
RDAR-WS, D. Castellano
RDAR-WSW, M. Ford
Picatinny Arsenal, NJ 07806-5000

Defense Technical Information Center (DTIC)
ATTN: Accessions Division
8725 John J. Kingman Road, Ste 0944
Fort Belvoir, VA 22060-6218

Commander
Soldier and Biological/Chemical Command
ATTN: AMSSB-CII, Library
Aberdeen Proving Ground, MD 21010-5423

Director
U.S. Army Research Laboratory
ATTN: AMSRL-CI-LP, Technical Library
Bldg 4600
Aberdeen Proving Ground, MD 21005-5066

Chief
Benet Weapons Laboratory, CCAC
Armament Research, Development and Engineering Center
U.S. Army Research, Development and Engineering Command
ATTN: AMSRD-AAR-AEW
Watervliet, NY 12189-5000

Director
U.S. Army TRADOC Analysis Center-WSMR
ATTN: ATRC-WSS-R
White Sands Missile Range, NM 88002

Chemical Propulsion Information Agency For contractor releasable report,
ATTN: Accessions
10630 Little Patuxent Parkway, Suite 202
Columbia, MD 21044-3204

GIDEP Operations Center
P.O. Box 8000
Corona, VA 91718-8000